5-2009

Magnetoelastic coupling in a quantum spin ladder

Jessica Lynn White
University of Tennessee

To the Graduate Council:

I am submitting herewith a thesis written by Jessica Lynn White entitled "Magnetoelastic coupling in a quantum spin ladder." I have examined the final electronic copy of this thesis for form and content and recommend that it be accepted in partial fulfillment of the requirements for the degree of Master of Science, with a major in Physics.

Janice L. Musfeldt, Major Professor

We have read this thesis and recommend its acceptance:

Accepted for the Council:
Carolyn R. Hodges

Vice Provost and Dean of the Graduate School

(Original signatures are on file with official student records.)

To the Graduate Council:
I am submitting herewith a thesis written by Jessica Lynn White entitled "Magnetoelastic Coupling in a Quantum Spin Ladder." I have examined the final electronic copy of this thesis for form and content and recommend that it be accepted in partial fulfillment of the requirements for the degree of Master of Science, with a major in Physics.

_____

Prof. Janice. L. Musfeldt, Major Professor

We have read this thesis
and recommend its acceptance:

_____
Prof. Norman Mannella

_____
Prof. Hanno H. Weitering

Accepted for the Council:

_____

Carolyn R. Hodges, Vice Provost and Dean of
the Graduate School

(Original signatures are on file with official student records.)

Magnetoelastic Coupling in a Quantum Spin Ladder

A Thesis

Presented for the

Master of Science Degree

The University of Tennessee, Knoxville

Jessica White

May 2009

Acknowledgments

I would like to thank my advisor, Professor Janice L. Musfeldt, for her valuable guidance, advice, and support through my duration in her laboratory. Thank you for all of your time and for being an excellent role model. I also thank Professors Hanno Weitering and Norman Mannella for serving on my committee and reviewing my work.

I would like to express my thanks to everybody in our research group during the past two years: Luciana Vergara, Xiaoshan Xu, Tatiana Brinzari, Ozge Gunaydin-Sen, Qi Sun, Henok Mikre, and Peng Chen for their collaboration, encouragement, discussions, and assistance. I would also like to thank Scott Crooker, John Singleton, Ross MacDonald, Mark Turnbull, Chris Landee, and Hans Christen for excellent collaboration and hard work on my project.

Finally, I would like to express my special thanks to my parents and friends for their love, care, and support.

Abstract

In this thesis, I present magnetic and optical property studies of a S = $\frac{1}{2}$ Heisenberg antiferromagnetic quantum system. The compound under investigation is a copper halide spin ladder, (2,3-dmpyH)$_2$CuBr$_4$. This material is attractive not only because of its rarity as a spin ladder with strong magnetic exchange along the rail, but because copper halides are good model materials for the copper oxide systems. Both temperature and magnetic field were used to tune the system. Magnetization was performed, allowing us to observe the experimental critical fields. These critical fields were in reasonable agreement with the theoretical models we extrapolated from strong rung spin ladder systems. Variable temperature optical experiments allowed us to assign the electronic excitations and showed that certain features (especially in the visible range) change shape or "sharpen" at low temperature. According to theoretical calculations, these excitations are caused by the $CuBr_4{}^{2-}$ chromophore of the system. Using the magnetic field, we were able to drive the antiferromagnetic (AFM) to ferromagnetic (FM) transition and see a spectral shift, resulting in a color change. This shift is too large to be a result of either Zeeman splitting or g factor effects, and is interpreted as an effect of magnetoelastic coupling. Finally, the magneto-optical data was correlated with the magnetization data. By plotting the absorption contrast (the integral of the absolute absorption difference) with the magnetization, we saw that the optical properties track the magnetization data with a small lag. The lag that we see is attributed to a slower lattice response in the system. Although we also discuss the results in terms of Cu^{2+}

moment saturation, spin canting, and fluctuation canting. The optics, thus, are sensitive to the antiferromagnetic to ferromagnetic transition, and distortion of the "ladder" couples the intramolecular effects with the intermolecular effects.

Contents

List of Tables

List of Figures

Chapter 1

Introduction: Properties of a Rare "Strong Rail" Quantum Spin Ladder

Since the discovery of high-temperature superconductivity in lightly doped antiferromagnets in the late 1980s, a burgeoning field has developed around the study of low-dimensional quantum magnets. [1–3] These systems have very interesting physical properties that are tunable with temperature, pressure, and magnetic field. One of the most fundamental magnetic field-induced transitions involves driving an antiferromagnet to the ferromagnetic state. There are many other types of field-induced transitions, including those to the ferrimagnetic and metamagnetic states. Here, we will focus on the antiferromagnetic (AFM) to ferromagnetic (FM) transition due to its simplicity and importance. Quantum Heisenberg spin ladders, a type of low-dimensional quantum magnet, are some of the most interesting and well-studied systems. In addition to being attractive in their own right, they are excellent models for understanding copper oxides. Unfortunately, cuprates have high energy scales, making them very difficult to study using conventional powered and pulsed magnets. Due to lower exchange interactions, it is possible to reach magnetization saturation in the copper halides, making them excellent model compounds for copper oxides. [4]

A spin ladder is a structural ladder that exhibits quantum magnetic effects. Although structural ladders are common, physical manifestations of a spin ladder are uncommon. An ideal spin ladder has a ratio of $J_\perp/J_\parallel = 1$, where the ratio of $J_\perp/J_\parallel$ is a "sliding scale" of magnetic interactions. When $J_\perp \gg J_\parallel$, dimers are formed, and when $J_\parallel \gg J_\perp$, linear chains are formed with no rail interaction in the limit of $J_\perp \to 0$. Physical manifestations of a spin ladder with a ratio near or equal to 1 are very rare. The ratio is what initially attracted us to Bis 2,3-dimethylpyridinium tetrabromocuprate [$(2,3\text{-dmpyH})_2CuBr_4$].

Our system is a spin ladder, with crystal packing characterized by the formation of a ladder with rungs and rails formed between the bromine atoms via a crystallographic inversion center (Figure 1.1). [4] For $(2,3\text{-dmpyH})_2CuBr_4$, $J_\parallel$ = -8.42 K and $J_\perp$ = -4.34 K, and has a $J_\perp/J_\parallel$ ratio of 0.52. [4] Unlike most magnetic spin ladders which have strong rung-rung ($J_\perp$) interactions, this compound has strong rail-rail ($J_\parallel$) interactions. [4] Unpublished wave-vector and energy dependent magnetic neutron scattering data confirms the presence of a two-leg spin ladder. [4–6]

In order to investigate the interplay between charge, structure, and magnetism in a tunable spin ladder material, we measured the magnetization and energy-dependent optical and magneto-optical properties of $(2,3\text{-dmpyH})_2CuBr_4$. Magnetization showed two critical fields in the system. The first critical field occurred at 2.8 T, where the spin gap closes due to the Zeeman energy exceeding the gap energy, and the second at 29 T, where the saturation magnetization occurs. The lack of other significant features in the experimental magnetization shows that there is absence of additional significant magnetic exchange within the molecules, other than those interactions that form the ladder. [4] Complementary optical and magneto-optical spectroscopies show that the electronic response is dominated by the excitations of the $CuBr_4{}^{2-}$ chromophore and that an applied field modifies the color properties of the triplet centered at $\sim$ 2.2 eV and on the leading edge of the $1A_1 \to 6A_1$ band at $\sim$ 3.2 eV. [7] Strikingly, the optical contrast tracks the magnetization, a result that we

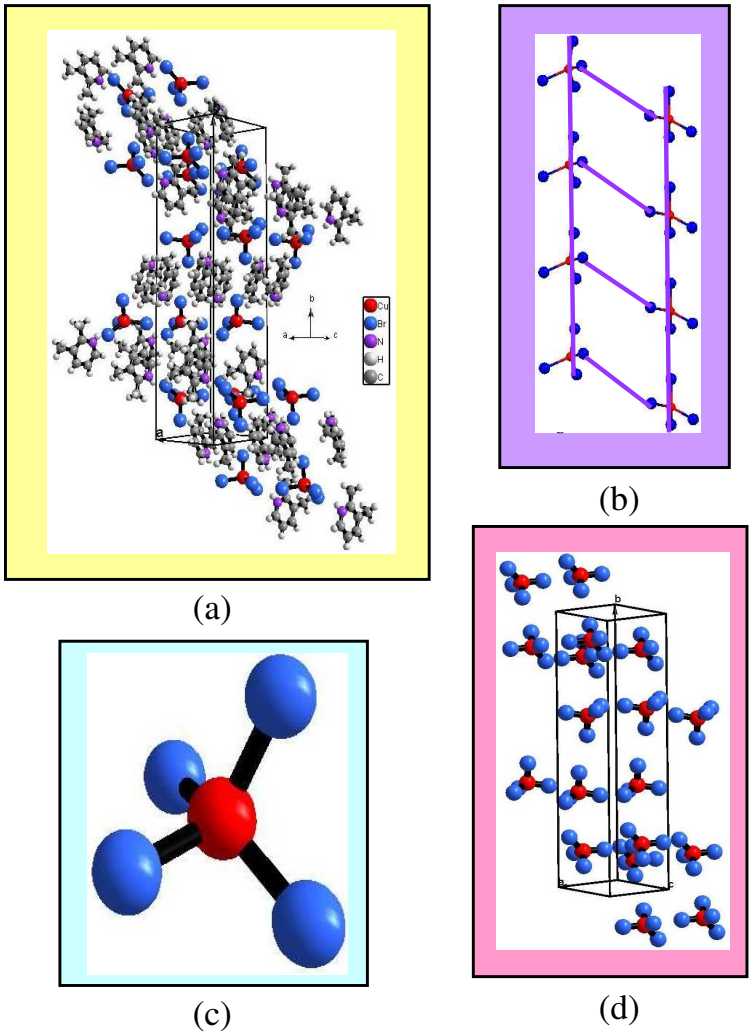

Figure 1.1: Various views of $(2,3\text{-dmpyH})_2CuBr_4$ including (a) the full molecule, (b) the chromophore "ladder", (c) a close-up view of the quasi-tetrahedral C_{2v} chromophore, and (d) a 3-D view of the structure minus the organic counter-ion.

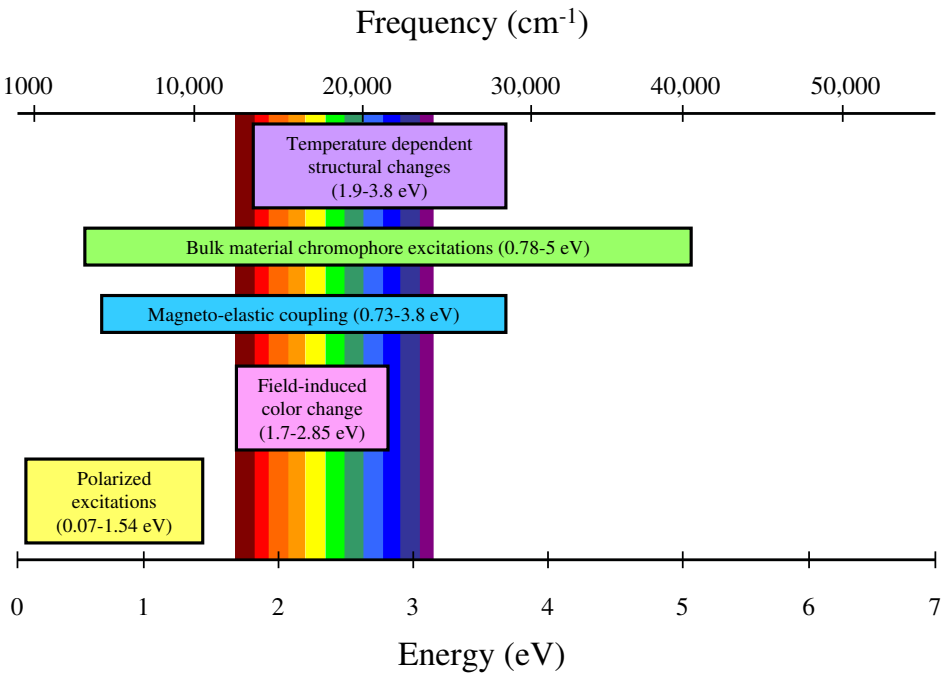

Figure 1.2: A close-up view of the areas of the electromagnetic spectra used in our experiments.

discuss in terms of charge-spin coupling mediated by local lattice distortions. This tracking shows that the magneto-optical data is sensitive to the AFM-FM transition. The saturation of the optical contrast shows a small lag, due to a slower lattice response. A similar effect is seen in direct magnetoelastic measurements of $[Cu(HF_2)(pyz)_2]BF_4$, [8] and the correlation of intermolecular (magnetization) and intramolecular (optical) effects points toward a magnetoelastic mechanism. Our scientific findings are showcased in Figure 1.2.

Since many of the copper oxide superconductors contain layers of S = $\frac{1}{2}$ Cu(II) ions, understanding the magnetic properties of our system, a S = $\frac{1}{2}$ quantum Heisenberg antiferromagnet, gives futher insight to the phase transitions and critical phenomena of these unique systems. [9] The color change seen in our system could also be indicative to the behavior of some cuprate superconductors, due to a spectral shift of the absorption in the visible range. [10, 11] Thus, the uniqueness of our copper halide system as a rare strong rail spin ladder gives an alternative insight into the copper oxide systems.

The rest of this thesis is organized as follows. Chapter 2 describes the various optical and magnetization techniques used throughout this work. Chapter 3 gives a literature survey of copper oxides in their varying forms, including those that are doped with other transition metals and those employing ligand substitution. Chapter 4 summarizes our magnetic properties investigation of $(2,3\text{-dmpyH})_2CuBr_4$. Chapter 5 focuses on our optical experiments. Chapter 6 summarizes our findings. Table 1.1 summarizes our findings, and Figure 1.3 gives a graphical summary of our work.

Table 1.1: Scientific problems and my contributions to the field.

Model System	Scientific Problems	Our Scientific Findings
$(2,3\text{-dmpyH})_2CuBr_4$	• Identification of critical magnetic fields • Temperature - induced structural change • Optical contrast through magnetic ordering transition	• AFM to FM transition can be driven by magnetic field • Experimental: $H_{C1} = 2.8$ T; $H_{C2} = 29$ T; $\Delta = 4.27$ K; values in good agreement with extrapolated "strong rung" theoretical models • Low temperature/high field studies show structural changes to the $CuBr_4{}^{2-}$ chromophore excitations from 1.75-3.75 eV • Optical properties sensitive to AFM-FM transition, with a small lag compared to the magnetization • Visible color change, due to field-induced changes in magnetoelastic coupling, causing distortion of the $CuBr_4{}^{2-}$ chromophore

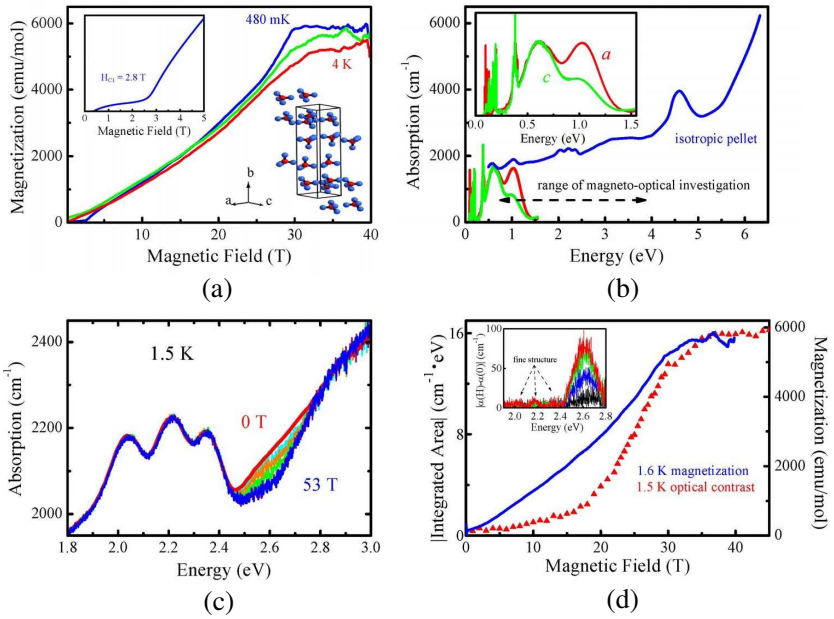

Figure 1.3: Summary of our findings, including (a) the magnetization of $(2,3\text{-dmpyH})_2CuBr_4$, (b) optical absorption of $(2,3\text{-dmpyH})_2CuBr_4$, (c) a close-up view of the absorption as a function of field, and (d) a comparison of magnetization with integrated absolute absorption difference.

Chapter 2

Methods

2.1 Materials of Interest

2.1.1 Synthesis Bis 2,3-Dimethylpyridinium Tetrabromocuprate Crystals

Single crystal samples of bis 2,3-dimethylpyridinium tetrabromocuprate were grown by Mark Turnbull and Chris Landee at Clark University. Copper (II) Bromide (2.172 g, 9.72 mmol) was dissolved in 30 mL of water, resulting in a bluish green mixture. Following filtering to remove insoluble trace material, aqueous HBr (21.6 mL of 9 M) was added to 2,3 dmpy (2.084 g, 19.4 mmol) to give an pale orange solution. The combined solution, (2,3 dmpyH)Br was then added slowly to the stirring solution of $CuBr_2$ to give a dark red/black mixture. The solution was then placed in a dessicator, with crystal formation being observed at three weeks and harvested at five weeks. The crystals were washed with *tert*-butanol, and appeared opaque dark purple with an elongated rectangular prismal shape. [4]

Crystal selection is two-fold. First, the crystals are examined under a microscope, looking for a crystal with few inclusions and a shiny, flat surface. Due to the low level of reflectance, large crystals are very useful, as the increased surface area allows for a higher reflective signal.

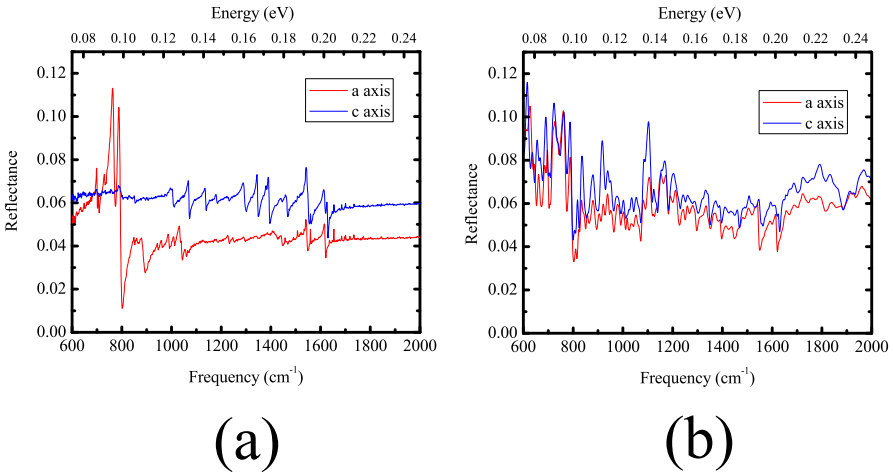

Figure 2.1: Spectra of good (a) and bad (b) crystal samples.

The second part of crystal selection involves examining the polarized middle infra-red spectra with the Fourier transfer infra-red spectrometer. In a "good" crystal, certain features appear as an extension of the earlier electronic structure, between 1000-1600 cm^{-1} (0.12-0.20 eV). In a "bad" crystal, this structure appears scattered looking, lacking the signature shape, indicating disorder. Figure 2.1 shows example spectra. High quality crystals were selected for our experiments. Figure 2.2 shows an example.

2.1.2 Pellet Preparation

Isotropic pressed pellets were made with a mixture of $(2,3\text{-dmpyH})_2CuBr_4$ and KCl powder. A small, good quality crystal was fractured using a mortar and pestle, and then appropriate amounts of 24 hour dried and annealed KCl and sample were combined and mixed to form a homogeneous powder. The powder was then tranferred into the die and placed in the hydraulic press. It stays in the press at 9 tons under vacuum for ten minutes. The final concentration used in our pellet was 0.77 percent sample by weight. The measured thickness of the pressed pellet was 0.08001 cm. Figure 2.3 shows a photograph of a prototype pellet.

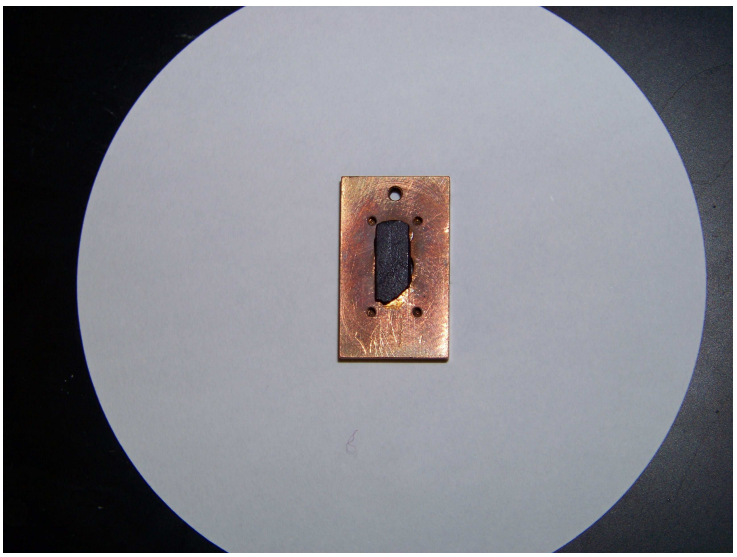

Figure 2.2: A single crystal sample mounted in a reflectance sample holder.

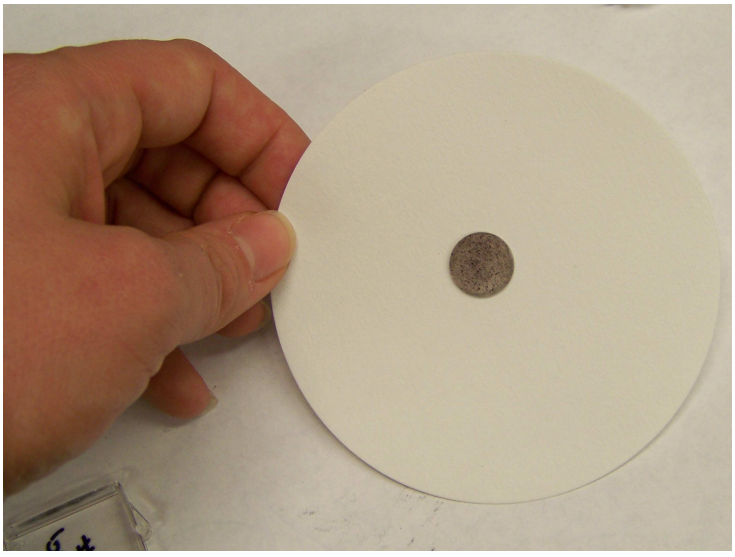

Figure 2.3: A pressed isotropic pellet with a concentration of 0.77 percent.

2.2 Introduction to Magneto-optics

When a solid is subject to electromagnetic radiation of intensity I_0, the intensity of this beam is attenuated after passing through the sample. Several processes, such as absorption, reflectance, and scattering, contribute to the attenuation. Infrared and optical spectroscopies analyze reflectance or transmittance of the sample as a function photon energy. If infrared and optical reflectance is done over a wide frequency range, a Kramers-Kronig analysis can correlate the measured data to the dielectric function, $\epsilon(\omega)$. [12] When the spectroscopy is done by transmittance, we are able to calculate the absorbance with our knowledge of the isotropic pellet thickness and loading, coupled with measurements done on several spectrometers with different light sources and detectors. This chapter will examine the different techniques utilized in the experimental and theoretical parts of our research.

2.3 Optical Properties of Solids

2.3.1 Maxwell's Equation and Optical Constants

The theoretical description of the interaction of radiation with matter and the analysis of the experimental results are based on Maxwell's equations and on their solution for time-varying electric and magnetic fields. In the long wavelength limit, the propagation of electromagnetic wave can be described by the macroscopic Maxwell's equations: [12]

$$\nabla \cdot \mathbf{D} = 4\pi\rho^{ext} \tag{2.1}$$

$$\nabla \times \mathbf{E} = -\frac{1}{c}\frac{\partial \mathbf{B}}{\partial t} \tag{2.2}$$

$$\nabla \cdot \mathbf{B} = 0 \tag{2.3}$$

$$\nabla \times \mathbf{H} = \frac{1}{c}\frac{\partial \mathbf{D}}{\partial t} + \frac{4\pi}{c}\mathbf{J}^{cond} + \frac{4\pi}{c}\mathbf{J}^{ext}, \tag{2.4}$$

where $\mathbf{E}$ and $\mathbf{H}$ are the electric and magnetic fields, $\mathbf{D}$ and $\mathbf{B}$ are the displacement field and magnetic induction, $\mathbf{J}^{cond}$ are free-current density, and $\mathbf{J}^{ext}$ and ρ^{ext} are current and charge density induced by external force. In an anisotropic medium, the polarization and induced currents generally lie in a direction different from that of the electric field. We can represent the dielectric function as a tensor to solve this problem. For simplicity, in the isotropic media and within the linear approximation, we can assume

$$\mathbf{D} = \epsilon \mathbf{E} \tag{2.5}$$

$$\mathbf{B} = \mu \mathbf{H} \tag{2.6}$$

$$\mathbf{J}^{cond} = \sigma \mathbf{E}, \tag{2.7}$$

where ϵ is the dielectric function, and σ is the optical conductivity, and μ is the magnetic permeability. Here both ϵ and σ are scalar quantities rather than tensors for the isotropic and homogeneous media.

The complex refraction index [12]

$$N(\omega) = n(\omega) + i\kappa(\omega),$$

and the complex dielectric function

$$\epsilon(\omega) = \epsilon_r(\omega) + i\epsilon_i(\omega),$$

where n and κ are the refractive index and the extinction coefficient, and $N(\omega)$ and $\epsilon(\omega)$ are related by the following equation

$$N(\omega) = \sqrt{\epsilon(\omega)}. \tag{2.8}$$

Finally, solving Maxwell's equation 2.1-2.4 for a plane wave

$$\mathbf{E} = \mathbf{E_0} exp[i(\mathbf{q} \cdot \mathbf{x} - \omega t)] \tag{2.9}$$

gives the following relation,

$$\epsilon(\omega) = 1 + \frac{i\sigma(\omega)}{\omega\epsilon_0}, \tag{2.10}$$

or

$$\epsilon(\omega) = \epsilon_1(\omega) + i\epsilon_2(\omega) = \epsilon_1(\omega) + \frac{4\pi i\sigma_1(\omega)}{\omega}, \tag{2.11}$$

where $\sigma_1(\omega)$ is the frequency dependent (optical) conductivity. In the case of weak absorption, $\epsilon_1 = n^2 - k^2 \approx n^2$, and $v \approx c/n$, the absorption coefficient α can be written as

$$\alpha = \frac{4\pi\sigma}{\epsilon_1 v} = \frac{4\pi\sigma}{nc}. \tag{2.12}$$

When measuring a sample in transmittance, it is also possible to determine α independently. Using the equation

$$\alpha = -\frac{1}{hd} ln(T) \tag{2.13}$$

we are able to calculate the absorption. In the equation, h represents sample loading (weight percent of sample), and d is the thickness of the pellet measured in centimeters. T signifies the transmittance level.

2.3.2 Lorentz and Drude Models

The dielectric function can be modeled by three parts:

$$\epsilon = \epsilon_\infty + \epsilon_{free} + \epsilon_{bound}, \tag{2.14}$$

where ϵ_{free} is the contribution from free electrons, and ϵ_{bound} is contributed from bound carriers. In this study, we will be interested primarily in the bound carriers.

The model to describe the contribution of free carriers to the dielectric function is called the Drude model, and the contribution of bound electrons is modeled with a Lorentz oscillator. Both models are essentially deducted from the dielectric function of a harmonic oscillator with frequency ω_0 responding to an electromagnetic field, with ω_0=0 for the Drude model. [12]

The form of the Lorentz dielectric function is:

$$\epsilon = \epsilon_\infty + \sum \frac{\omega_{pj}^2}{\omega_j^2 - \omega^2 - i\omega\gamma_i}_j , \tag{2.15}$$

where the plasma frequency

$$\omega_p = \sqrt{\frac{4\pi N e^2}{m}}, \tag{2.16}$$

and ω_j and γ_j are the resonant frequency and damping constant, respectively, of the j^{th} Lorentzian oscillators.

From Eqs. 2.15, taking ω_j=0, we have the form of the Drude dielectric function

$$\epsilon_D(\omega) = \epsilon_\infty - \frac{\omega_p^2}{\omega^2 + \frac{i\omega}{\tau}} \tag{2.17}$$

where τ=1/γ is the mean free time between collisions.

2.3.3 Fitting Techniques

The PeakFit program was used to analyze the bound carrier excitations. Model oscillator fitting the peaks is a way to further determine the relationship between the the spectral peaks and the Lorentz Oscillator. Peakfit allows for three types of fits: Gaussian, Lorentzian, and Voigt. The Gaussian fits, with their symmetric shape, are often due to instrument response.

The equations used to fit the Gaussian are

$$y = a_0 exp[\frac{-1}{2}(\frac{x - a_1}{a_2})^2], \tag{2.18}$$

where a_0 = amplitude, a_1 = center, and a_2 = width, (greater than 0) and

$$y = \frac{a_0}{\sqrt{2\pi}a_2} exp[\frac{-1}{2}(\frac{x - a_1}{a_2})^2], \tag{2.19}$$

where a_0 = area, a_1 = center, and a_2 = width (greater than 0).

The following equations are used to determine Lorentz peaks. The equation

$$y = \frac{a_0}{1 + (\frac{x-a_1}{a_2}^2)}, \tag{2.20}$$

represents Lorentzian amplitude, and the equation

$$y = \frac{a_0}{\pi a_2[1 + (\frac{x-a_1}{a_2})^2]}, \tag{2.21}$$

represents the Lorentzian area equation. In the above equations, a_0 = area, a_1 = center, and a_2 = width (greater than 0).

When fitting peaks, it is possible to use the Lorentz mode, which does not converge to a single mean and standard deviation as the size of the sample set increases. It is also not uncommon for a portion of the fitted Lorentzian's area to lay outside the range of the spectrum. Due to this problem, we use the Voigt mode to fit our peaks.

The Voigt function involves a convolution of the Gaussian and Lorentzian models. When using the Voigt mode, it is possible to vary both width and shape, since they affect one another. In the end, the Voigt oscillator is slightly better, as it is able to mimic the shape of observed excitations much better than Lorentz. The Voigt mode equations are as follows:

$$y = \frac{a_0 \int \frac{exp(-t^2)}{a_3^2 + (\frac{x-a_1}{a_2} - t)^2}}{\int \frac{exp(-t^2)}{a_3^2 + t^2} dt}, \tag{2.22}$$

and

$$y = \frac{a_0}{\sqrt{\pi} a_2} \int \frac{exp(-t^2)}{a_3^2 + (\frac{x-a_1}{a_2} - t)}, \tag{2.23}$$

where a_o = amplitude, a_1= center, a_2= width, and a_3=shape. To calculate the Voigt amplitude with Gaussian/Lorentzian widths, we used the equation

$$y = \frac{a_o \int \frac{exp(-t^2)}{\frac{a_3^2}{2a_2^2} + (\frac{x-a_1}{\sqrt{2}a_2} - t)^2}}{\int \frac{exp(-t^2)}{\frac{a_3^2}{2a_2^2} + t^2}}, \tag{2.24}$$

where a_0 = amplitude, a_1=center, a_2=width one (Gaussian), and a_3=width two (Lorentzian). To solve for the Voigt area, a different equation is necessary. Here we employ

$$y = \frac{a_o}{\sqrt{2\pi} a_2} \int \frac{exp(-t^2)}{\frac{a_3^2}{2a_2^2} + (\frac{x-a_1}{\sqrt{2}a_2} - t)^2}, \tag{2.25}$$

where a_0 is area, a_1 is the center, and a_2 and a_3 are the Gaussian and Lorentzian widths, respectively, Peakfit was able to give a standard error and confidence limits for the computation of each of the widths.

2.4 Spectrometers

2.4.1 Bruker Equinox 55 IR Microscope

The Bruker IR Scope II is designed for accurate measurement of micro samples, or small areas on larger samples. In our lab, Bruker IRscope II combined with Bruker Equinox 55

Table 2.1: Bruker IRscope II operating parameters

Beam splitter	Detector	Range (cm^{-1})	Range (eV)
KBr	MCT	600-8000	0.07-1.0
Quartz	InPb	7500-12500	0.93-1.55
Quartz	Si diode	12300 -16000	1.53-1.98

FTIR spectrometer can be used to obtain the spectrum from the middle-infrared to visible range. It is ideal for small crystals, small edges of a crystal, and checking the absolute reflectance level obtained on the other instruments.

Bruker Equinox 55 FTIR spectrometer is equipped with a Globar source, two beam-splitters, and a DTGS detector. It has an external port to transfer the incident light to the IRscope II. IRscope II has three objectives (4×, 15×, and 30×), and several detectors (MCT, InPb, and Si diode) to cover the energy range from 600-16000 cm^{-1} (0.07-1.98 eV).

Figure 2.4 shows the optical path of Bruker IRscope II. The IRscope II can measure reflectance or transmission of the sample by changing the orientation of mirror 22. The infrared or visible mode can be chosen depending on the orientation of mirror 3 (reflectance mode) or 17 (transmission mode). The detector can be changed by flipping mirror 13. Table 2.1 lists the operating parameters of Bruker Equinox 55 FTIR spectrometer combined with IRscope II. The spectrometer is operated under N_2 purge.

2.4.2 Perkin-Elmer λ-900 Spectrometer

The Near Infra-Red/Visible/Ultraviolet spectra in this thesis were measured on the Perkin-Elmer λ-900 Spectrometer. The Perkin-Elmer λ-900 Spectrometer features an all-reflecting, double-monochromator, double-beam optical system. The energy range covered by the λ-900 Spectrometer is 3300-190 nm ($\approx$ 3000-52000 cm^{-1})(0.37-6.45 eV). The spectrometer is

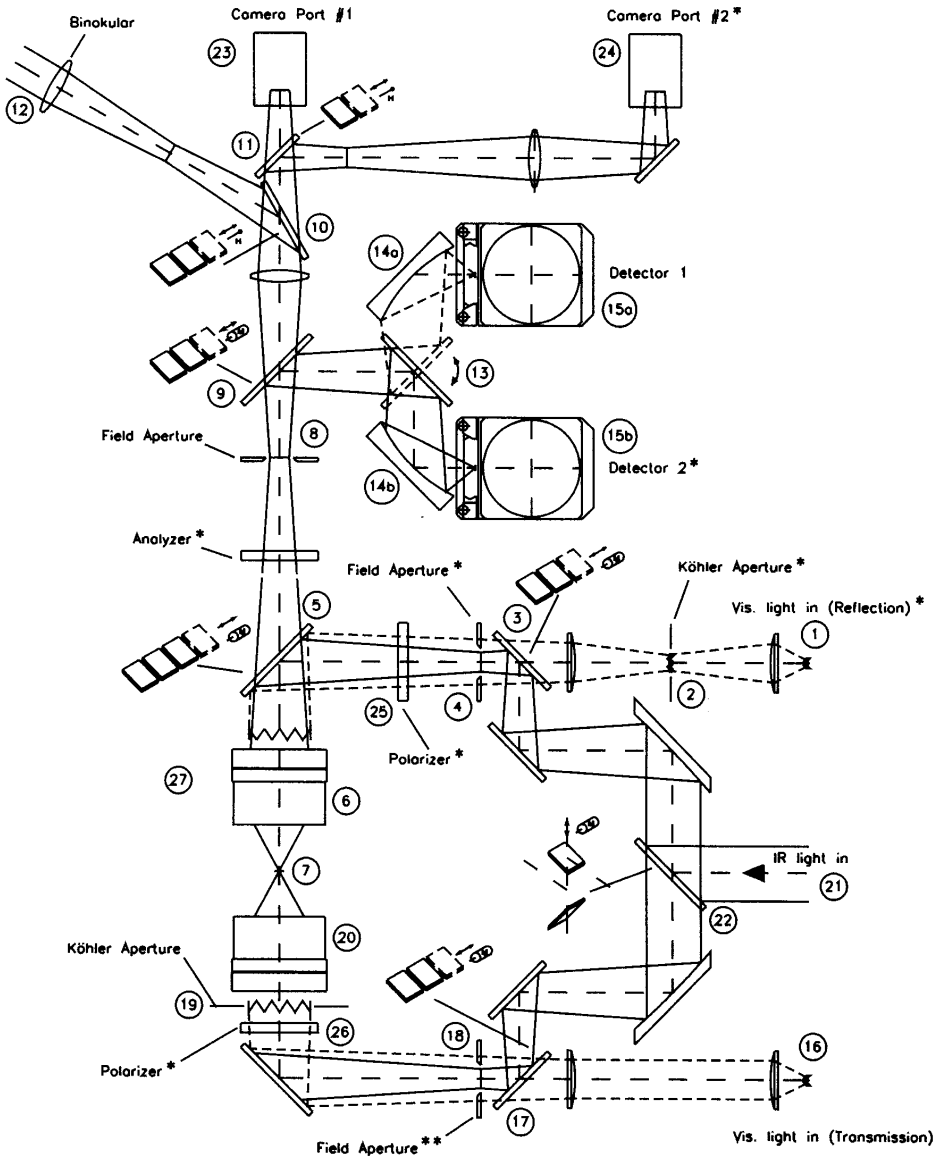

Figure 2.4: Optical path diagram of Bruker IRscope II.
1,16-visible light source; 2,19- visible light aperture; 3,22- motorized switch mirror; 4,18- optional iris or knife edge aperture; 5,9,10,17- beamsplitter changer; 6- Objective lens; 7- Sample; 8- Iris or knife edge aperture which defines the area of sample analyzed; 12- binocular eyepiece; 13- two position detector selection mirror; 14- mirror routing to detector; 15- detector; 20- condenser; 21- IR beam (from spectrometer); 23,24-camera port; 25,26,27- polarizer.

operated under N_2 purge. The optical system is depicted schematically in Figure 2.5.

There are two radiation sources, a deuterium lamp and a halogen lamp. Halogen lamp is used for Near Infra-Red and Visible range, and deuterium lamp is used for Ultraviolet range. Source change is controlled by flipping mirror M1. The radiation of source is reflected by mirror M2, M3, and passes optical filter FW. Then, the beam is brought in monochromator I through M4, slit SA, and M5. Depending on the desired wavelength range, the collimated radiation beam strikes either the 2400 lines/mm grating or the 1200 lines/mm grating. The rotation position of the grating effectively selects a segment of the spectrum, reflecting this segment to mirror M5, to go through the exit slit, and enter Monochromator II. The advantage of the double-monochrometer is to maintain high spectral purity with an extremely low stray radiation content. The automatic grating change during monochromator slewing avoids the time-consuming re-alignment of the optics pathway due to the monochromator change.

The double beam is achieved via the chopper assembly C. As the chopper rotates, a mirror segment, a window segment and two dark segments are brought alternately into the radiation beam. When a window segment enters the beam, radiation passes through to mirror M9 and is then reflected via mirror M10 to create the reference beam (R). When a mirror segment enters the beam, the radiation is reflected via mirror M10′ to form the sample beam (S). When a dark segment is in the beam path, no radiation reaches the detector, permitting the detector to create the dark signal (D). Then, the measured spectrum is expressed as

$$spectrum = (S - D)/(R - D).$$

Two detectors are used in the Perkin-Elmer λ-900 spectrometer. A photomulitplier (PM) is used in the UV/Vis range while a lead sulfide (PbS) detector is used in the NIR range. Detector change is automatic by rotating mirror M14 during scans. Table 2.2 shows the

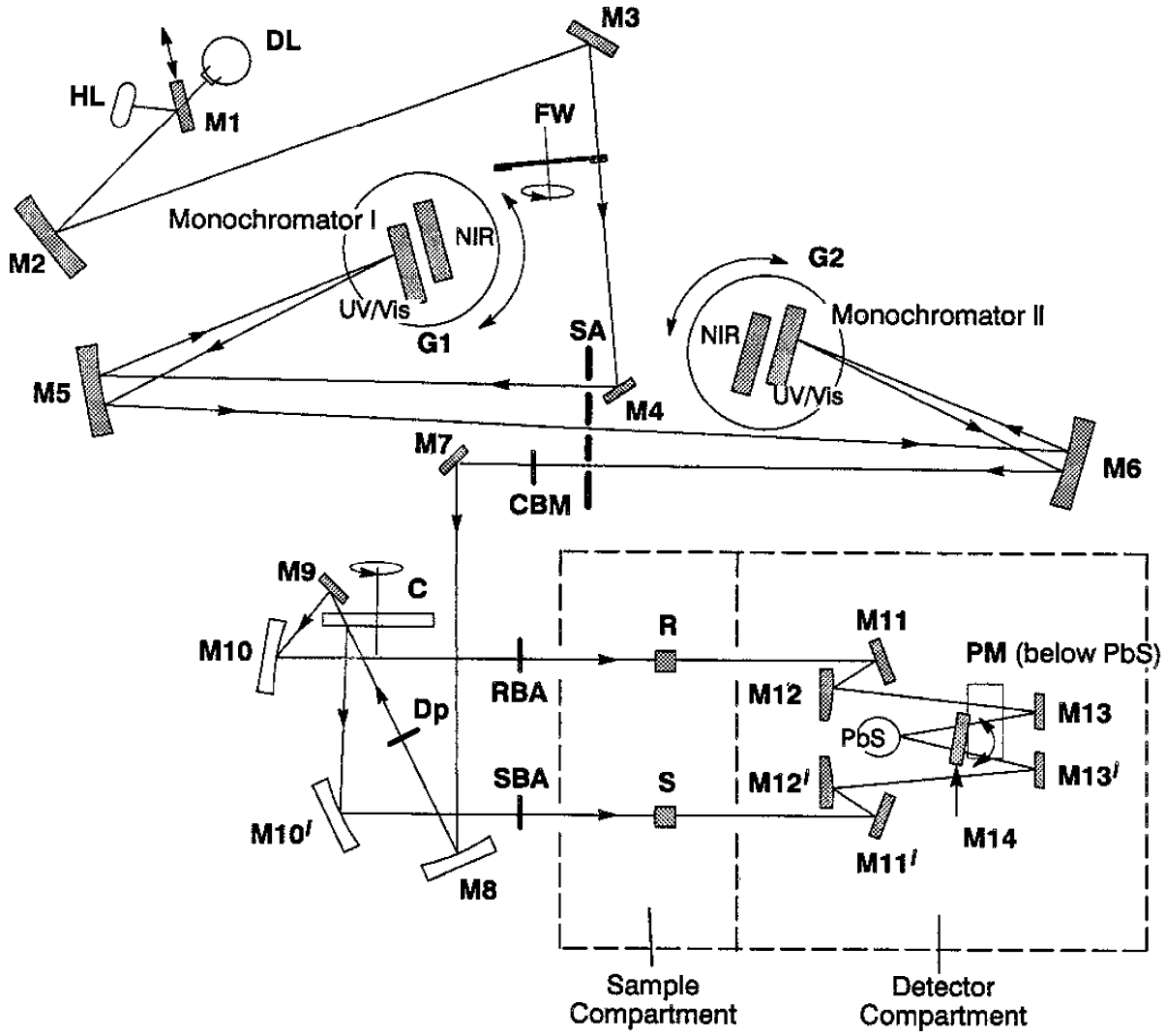

Figure 2.5: Optical layout of Perkin-Elmer λ-900.

Table 2.2: λ-900 operating parameters

Monochromator	Source	Detector	Range (cm^{-1})	Range (eV)
Holographic Gratings	Halogen Lamp	PbS	3100-14250	0.38-1.77
Holographic Gratings	Halogen Lamp	Photomultiplier	11240-31330	1.40-3.90
Holographic Gratings	Deuterium Lamp	Photomultiplier	31330-52000	1.40-6.45

operating parameters of the λ-900.

2.5 Transmittance and Reflectance Spectroscopy

2.5.1 Transmittance Stage

To measure the absolute absorbance spectrum, a transmittance stage (as shown in Figure 2.6) is used to bring the normal incidence light to an isotropic pellet or empty hole. The empty hole is usually used as a reference to obtain a baseline scan, then the transmittance spectrum of the sample of identical size is measured relative to the baseline. The absolute absorbance spectrum of the sample is obtained via calculation, using the thickness and loading of the sample:

$$\alpha(\omega) = \frac{-1}{hd} lnT(\omega). \tag{2.26}$$

The optical theory outlined in Section 2.3 is based on Maxwell's equations 2.1–2.4 and Eqs. 2.5–2.7. Eqs. 2.5– 2.7 are the material equations for an isotropic medium.

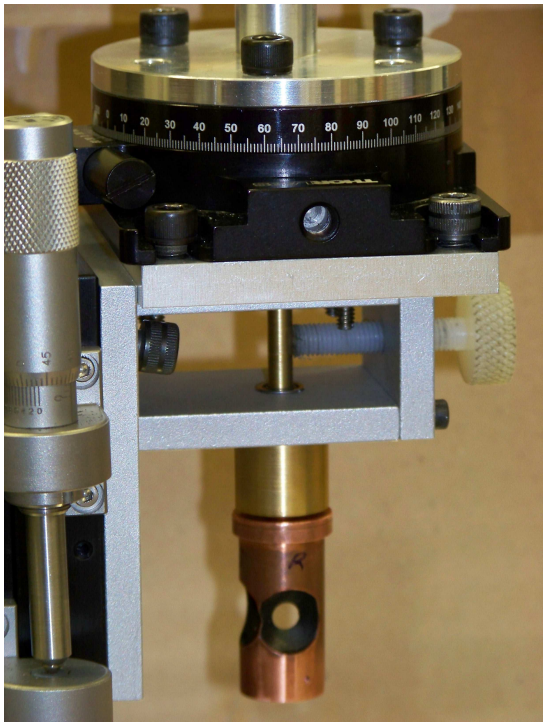

Figure 2.6: Transmittance sample holder for Perkin-Elmer λ-900.

2.5.2 Transmittance Measurements

Isotropic pellets were mounted and measured in the Perkin Elmer Lambda 900 Grating Spectrometer, over the range from 190-2500 nm (1.36-2.0 eV). Using the Scan-1 method, the spectral resolution was constant throughout the near infra-red and the ultraviolet/visible range at 2 nm. Variable temperature spectroscopies were carried out between 4.2-300 K using an open-flow helium cryostat and temperature controller, as described below.

2.5.3 Reflectance Measurements

Single crystal samples were mounted and measured in the Perkin Elmer Lambda 900 Grating Spectrometer and a Bruker Equinox 55. They were carried out over a range covering 190-2500 nm and 400-12500 cm^{-1} respectively. The spectral resolution was 2 cm^{-1} in the far and middle-infrared and 2 nm in the near-infrared, visible, and near-ultraviolet. Aluminum

mirrors were used as references for all measurements. Variable temperature spectroscopies were carried out between 4.2 and 300 K using an open-flow helium cryostat and temperature controller, as described below. Due to the degradation of the single crystal samples in the vacuum, we were unable to renormalize the data and perform Kramers-Kronig analysis, and further unable to explore the optical properties. We will not discuss reflectance techniques further.

2.6 Low-Temperature Measurements

2.6.1 Cryogenic Techniques

The low-temperature measurements were carried out with an open-flow cryostat. For the low-temperature experiments with the Perkin-Elmer λ-900, an APD LT-3-110 Heli-Tran Liquid Transfer Refrigeration system with dual temperature sensors together with a Lakeshore Model 330 temperature controller were adapted. The principles of operation are illustrated in Figure 2.7.

Cooling is accomplished by a controlled liquid He transfer through a transfer line to a heat exchanger adjacent to the sample interface. A needle valve at the end of the Heli-Tran transfer line permits precise control of the flow rate. The cooling rate can be regulated by changing the pressure of the supply dewar, adjusting the flowmeter and optimizing the position of the needle valve. It takes about 25 minutes to precool the system, and the lowest stable temperature obtained is $\sim$ 5 K. Figure 2.8 shows the shroud that holds the sample, when doing low temperature experiments.

To improve the thermal contact, crycon grease is placed between the cold stage of the cryostat and the sample holder, and the sample is mounted on the sample holder with rubber cement. There are two thermal sensors inside the cryostat, one is embedded in the tip of the cold stage, the other one is mounted on the sample holder. In this configuration, the

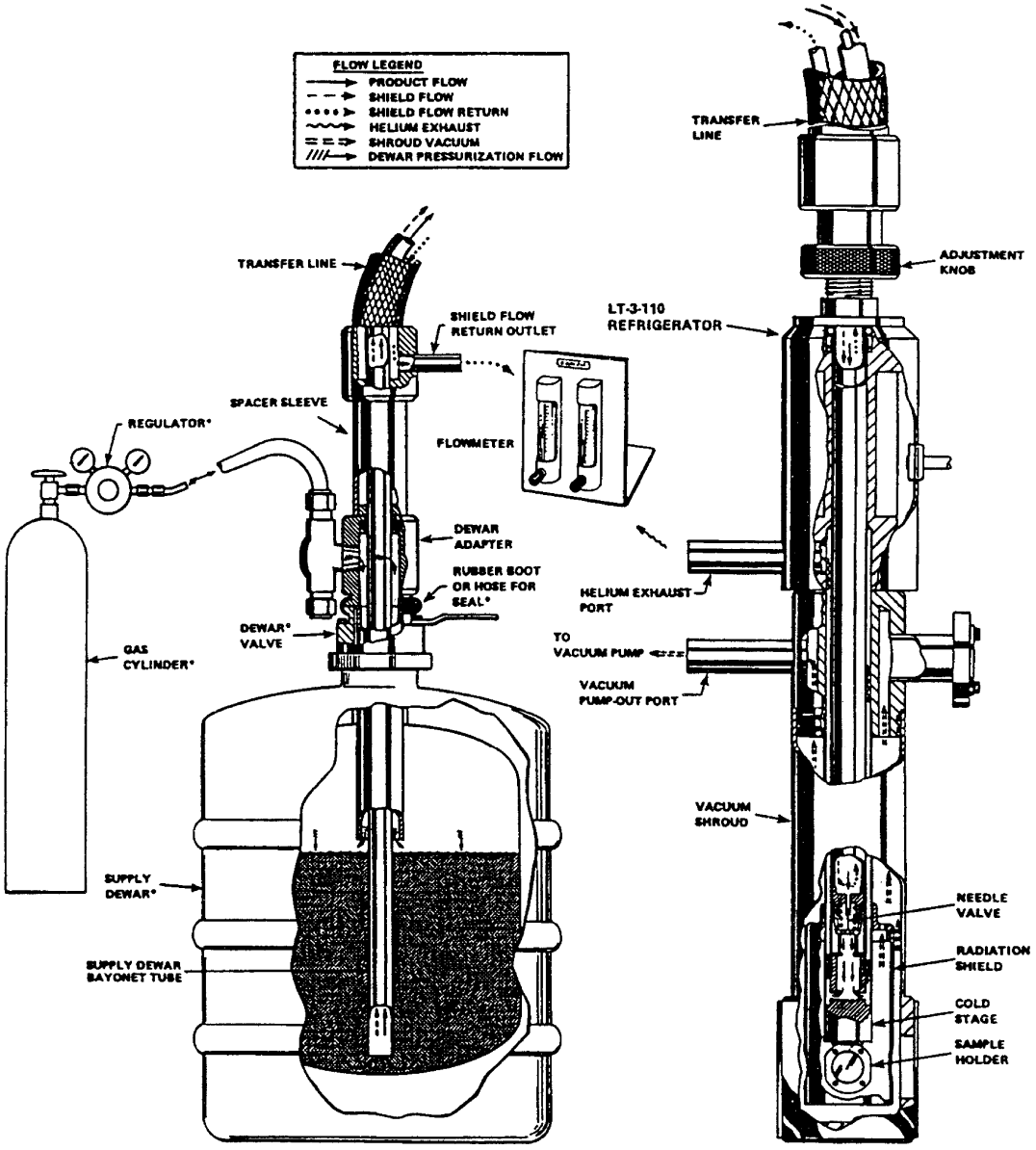

Figure 2.7: Set-up of LT-3-110 Heli-Tran liquid transfer line and cryostat.

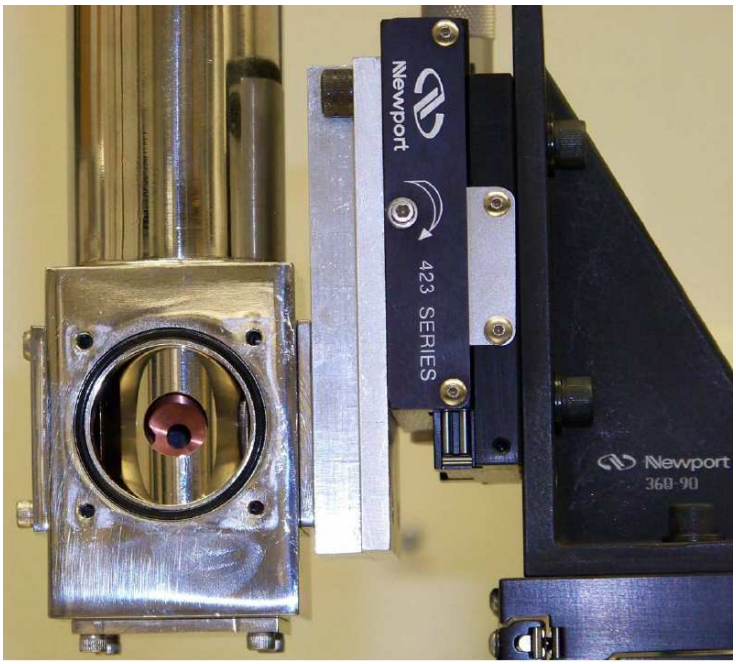

Figure 2.8: A view of a sample in the cryostat (transmittance mode).

temperatures provided by the two sensors allow us to estimate the real sample temperature.

2.6.2 High Magnetic Field Measurements

Experimental Set-up at the NHMFL

The National High Magnetic Field Laboratory (NHMFL) provides an opportunity to do magnet-related research. The world-class magnets and magneto-optics facilities at NHMFL make it possible to investigate the unusual nature of low-dimensional solids in very high magnetic fields. For more information, visit the website of NHMFL at *http://www.magnet.fsu.edu*. The information in this section is largely from NHMFL website and Refs. [13–15]. A hand-wound coil, similar to those found in the magnets used in magnetization, is shown below. Two concentric coils are wound in series. The inner coil is wound clockwise, and the outer is wound counterclockwise. Figure 2.9 shows the coil. The winding technique provides equal and opposite induced voltage. Therefore, when the sample is inserted into the coil, since the

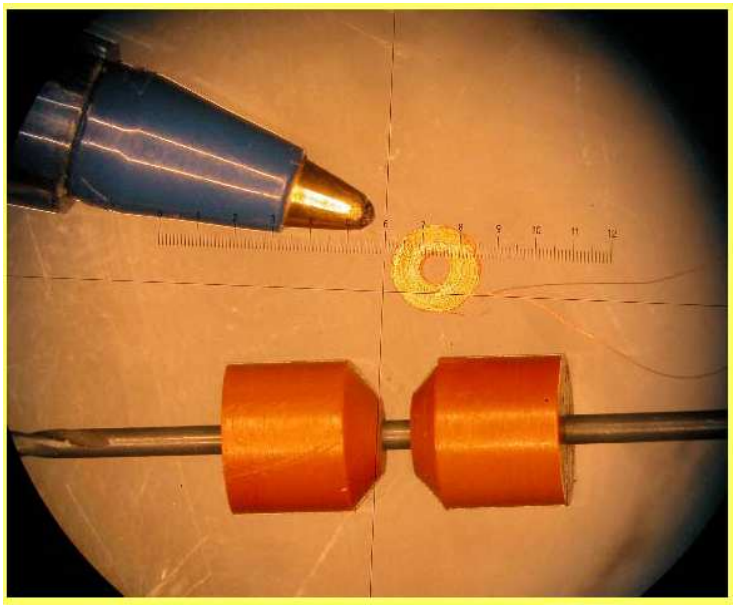

Figure 2.9: A close-up of a hand-wound magnetization coil. The coil shown here is a 1000 turn coil, with the inner coil of 650 turns and the outer coil of 350 turns. The tip of the pen gives perspective to the actual size of the coil.

induced voltage is zero, any voltage seen is due to the sample's magnetic moment.

Field Dependent Measurement of (2,3-dmpyH)$_2$CuBr$_4$

Magneto-optics were measured at Los Alamos on both isotropic pellets and single crystal samples. The pellet was cut and placed into the holder at the bottom of the probe. The probe was placed in the magnet and cooled. The pellet was then measured using a 60 T long-pulse magnet and a grating spectrometer, at a temperature of 1.4 K, a resolution of 0.26 nm and a wavelength range from 324-1692 nm (0.73-3.83 eV). When collecting the data, a pulse profile, as seen in Figure 2.10, was used to collect data. A shutter was also used, to allow the start of data acquisition to occur with the pulse of the magnet. The magnet pulses up and down from 0 to 53 T. The data is then checked on the upsweep and downsweep for hysteresis.

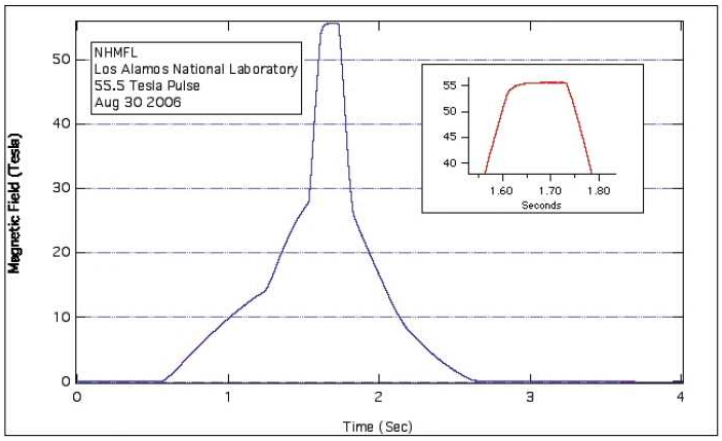

Figure 2.10: A schematic of the pulse in the 60 T long pulsed magnet at Los Alamos.

2.7 Magnetization

Single crystal magnetization was measured at Los Alamos using a hand-wound coil and 50 T short and mid pulse magnets. A single crystal was inserted into an ampule and then placed on the probe. Data was taken at 4.2 K, 1.6 K, and 480 mK. Low temperature data (480 mK) was the best for eluciating H_{c1} and H_{c2}. At each temperature and magnetic field strength, two shots were taken- one with the sample in the cryostat, and one with the sample out, to allow for the correction of the probe. Since the magnets at Los Alamos are not calibrated, upon our return to the University of Tennessee, we calibrated the magnetization data with the SQUID data obtained by Chris Landee and Mark Turnbull at Clark University to arrive at our final result.

The single crystal samples were also measured in reflectance geometry. To measure the single crystal, the sample was mounted on the probe with a polarizer and placed in the cryostat of a 50 T mid-pulse magnet. The single crystal's spectra was measured between 375 and 725 nm (0.3-0.58 eV), mimicking the area of activity in the isotropic pellet experiment. The magnet was pulsed twice, changing the orientation of the crystal to allow the a axis to be polarized both along and perpendicular to the rail. We then looked briefly at frequency shifts and oscillator strength changes in magnetic field, when plotting the single line spectra

at high field with the single line spectra at zero field. Later we examined the ratio of a single spectra at high field to the spectra at zero field. Not only was there a difinitive change in the spectral lines, there was an obvious difference between the two polarizations, confirming the hypothesis that there was directional dependence in the crystal. Owning to concerns about crystal degradation, these experiments cannot be regarded as definitive and are therefore discussed no further.

2.8 Color Rendering Techniques

Standard color rendering techniques are employed to visualize temperature- and field-induced spectral changes. [16,17] Through a Kramers-Kronig analysis, one can determine the extinction coefficient as a function of frequency, $\kappa(\omega)$. The absorption coefficient, α, is calculated as α=$4\pi\kappa(\omega)$. Here, the absorption coefficient data are "matched" with the effective absorption using a proportionality constant (which is typically on the order of the pellet thickness times the loading). The absorption coefficient needs to be normalized by a constant, K, to determine the effective absorption of the material. K is dependent on factors such as the mass fraction and thickness of the transmittance sample. This constant can be approximated by an examination of the transmittance of the material or by normalizing the absorption to a distinct value of color (assuming the color of the material is known). Once K is determined for a material, it is the same for all spectra and is not dependent on magnetic field or temperature. A comparison of the absorption coefficient to the effective absorption spectrum can be used to render color by integrating the product of the spectrum with the well-known XYZ color matching functions to determine the XYZ color values. [16] These XYZ values are converted into RGB color values and then inverted to determine the color of a material. [16] The final RGB values allow color rendering.

Chapter 3

Literature Review

3.1 Complex Materials and Their Energy Scales

Copper halide compounds are excellent foils for copper oxides. They display many of the same intriguing structures and properties of the oxides, but with overall lower energy scales. Thus, they are excellent model compounds. In this chapter we discuss structures and critical magnetic fields of some comparable materials.

Copper oxides are scientifically very interesting, but have very high critical fields and are difficult to saturate. There are two known solutions to this dilemma. The first is to use a halogen ligand, such as chlorine or bromine in place of oxygen. The other is to dope the material with another transition metal. Sometimes it is necessary to both dope the material and replace the oxygen. These strategies bring the critical magnetic field down to a feasible range, within reach of conventional superconducting, resistive and pulsed magnets. Although there are a variety of physically interesting low-dimensional oxides, few have attainable critical fields. Table 3.1 shows some materials of interest, and their experimental/theoretical critical magnetic fields.

Table 3.1: Similar Materials and Their Properties

Material	Structure	Critical Field	Reference
$LiCuVO_4$	planar CuO_2 1D chains ‖ b	40-50 T	[18]
$Sr_{2.5}Ca_{11.5}Cu_{24}O_{41}$	1D even-chain spin ladder	4416 T (estimate)	[19]
$SrCu_2O_3$	$\frac{1}{2}$ AFM spin ladder	4200 T (estimate)	[20]
$YBa_2Cu_3O_7$	2D CuO_2 planes	120 T ⊥, 250 T ‖	[21,22]
$YBa_2Cu_4O_8$	1D even-chain spin ladder	2240 T (estimate)	[19]
$CuGeO_3$	$\frac{1}{2}$ 1D AFM Heisenberg	253 T	[23]
$(DTTTF)_2Cu(mnt)_2$	organic $\frac{1}{2}$ spin ladder	460 T (estimate)	[24,25]
$(DTTTF)_2[Au(i\text{-}mnt)_2]$	organic $\frac{1}{2}$ spin ladder	314 T (estimate)	[25]
$(C_5H_{12}N)_2CuBr_4$	$\frac{1}{2}$ 2 leg spin ladder	14.6 T	[26]
$(5IAP)_2CuBr_4\ 2H_2O$	$\frac{1}{2}$ AFM spin ladder	10.4 T	[27]
$(C_5H_9NH_3)_2CuBr_4$	$\frac{1}{2}$ AFM spin ladder	24 T	[7,28]
$Cu_2(C_5H_{12}N_2)_2Cl_4$	$\frac{1}{2}$ AFM spin ladder	13.2 T	[29,30]
$CaCu_2O_3$	quasi-1D spin chain	297.5 T	[31]
$TlCuCl_3$	$\frac{1}{2}$ spin double chain systems	150 T	[32,33]
$KCuCl_3$	$\frac{1}{2}$ spin double chain systems	60 T	[32,33]
NH_4CuCl_3	$\frac{1}{2}$ spin double chain systems	29.1 T	[32]

3.1.1 Quantum Magnets and Spin Ladders

Quantum magnetism is one of the most active areas of research in condensed matter physics. Much attention is focused on low-dimensional spin systems, due to their large quantum effects, which occur as a result of Heisenberg coupling. [2,34] Different types of low-dimensional spin systems, such as 1-D spin chains, 2-leg spin ladders, 2-D square lattices, and 2-D rectangular lattices, are shown in Figure 3.1.

Spin ladders, with their interesting structural properties, will be the focus in this work. Spin ladders are a natural intermediate between one- and two-dimensional systems, giving them interesting structural properties. [2] Magnetic properties and quantum effects distinguish spin ladders from structural ladders. Some of the doped cuprate spin ladders are speculated to be high temperature superconductors, giving scientists an additional reason to fully understand these systems. [35]

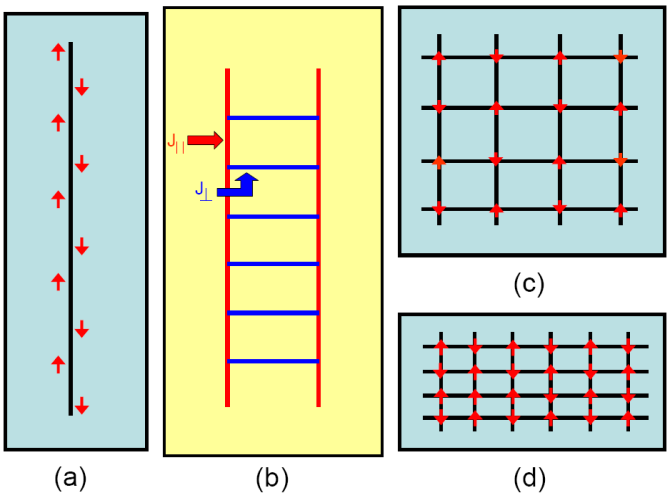

Figure 3.1: Structural representations of several low-dimensional systems, including (a) a 1-D spin chain, (b) a 2-leg spin ladder (where $J_{\parallel}$ and $J_{\perp}$ represent the rails and rungs of the ladder respectively), (c) a 2-D square lattice, and (d) a 2-D rectangular lattice.

The number of legs in the ladder greatly changes the properties. [36] A spin ladder can have any number of legs, although the 2-legged ladder is most common. Spin $\frac{1}{2}$ antiferromagnetic ladders have a finite gap in the spin excitation spectrum when there are an even number of legs, and no gap in the odd-leg case. [36]

An ideal spin ladder has a ratio of $J_{\perp}/J_{\parallel} = 1$, where the ratio of $J_{\perp}/J_{\parallel}$ is a "sliding scale" of magnetic interactions. When $J_{\perp} \gg J_{\parallel}$, dimers are formed, and when $J_{\parallel} \gg J_{\perp}$, linear chains are formed with no rail interaction in the limit of $J_{\perp} \rightarrow 0$. Figure 3.2 shows the sliding scale associated with spin ladders. Physical manifestations of a spin ladder with a ratio near or equal to 1 are rare. The ratio is what initially attracted us to the (2,3-dmpyH)$_2$CuBr$_4$ system. Our material is one of two spin ladder examples where the rail exchanges are stronger than the rung exchanges.

3.1.2 Doped Copper Oxides

Copper oxides are well-known superconductors, but due to their high saturation fields, they cannot be studied directly. In order to study their properties, they must be modified. By

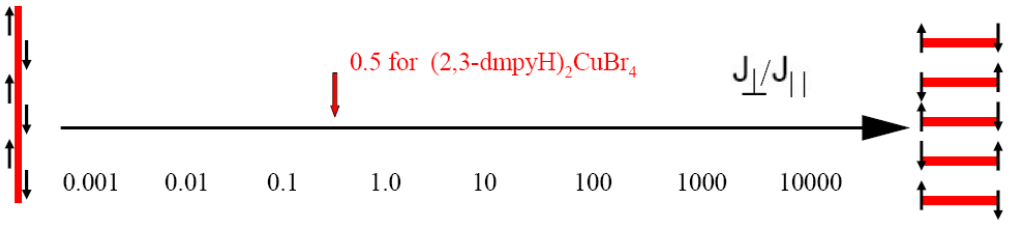

Figure 3.2: Sliding scale used for spin ladders: the $J_\perp/J_\parallel$ for (2,3-dmpyH)$_2$CuBr$_4$ is indicated at 0.5, placing it in a very interesting region.

doping these materials with an additional metal, the energy scales will, in theory, become lower. Metals, such as germanium, lithium, yttrium, barium, or vanadium have been doped into copper oxides to give varying results. Figure 3.3 shows several structures and critical magnetic fields of copper oxides.

The fields necessary to saturate these materials are extremely high, and not attainable with existing powered and pulsed magnets. The high fields necessary to saturate $CuGeO_3$, and $YBa_2Cu_3O_7$ show that although doping lowers the field, the field necessary to saturate is still not attainable. Table 3.1 shows that other doped materials, such as $SrCu_2O_3$ and $YBa_2Cu_4O_8$ are still estimated to need fields that are too high to reach with current magnet technology. On ther other hand, Table 3.1, shows that $LiCuVO_4$, $CuGeO_3$, and $YBa_2Cu_3O_7$ have been successfully saturated. Thus, doping is not always successful solution.

3.1.3 Copper Halides Present a Viable Alternative

Replacing the oxygen ligand with a halogen is an effective way to lower the critical magnetic field of copper-containing materials. As an example, consider the 5 d-orbitals in an octahedral field. The five d-orbitals split between the t_{2g} (nonbonding) and e_g (antibonding) levels. Oxygen is a strong field ligand, whereas bromine and chlorine are weak field ligands, according to the spectrochemical series, shown in Figure 3.4. [37] A strong field ligand causes a large d-orbital splitting energy (Δ_0), so the energy difference between the t_{2g} and e_g or-

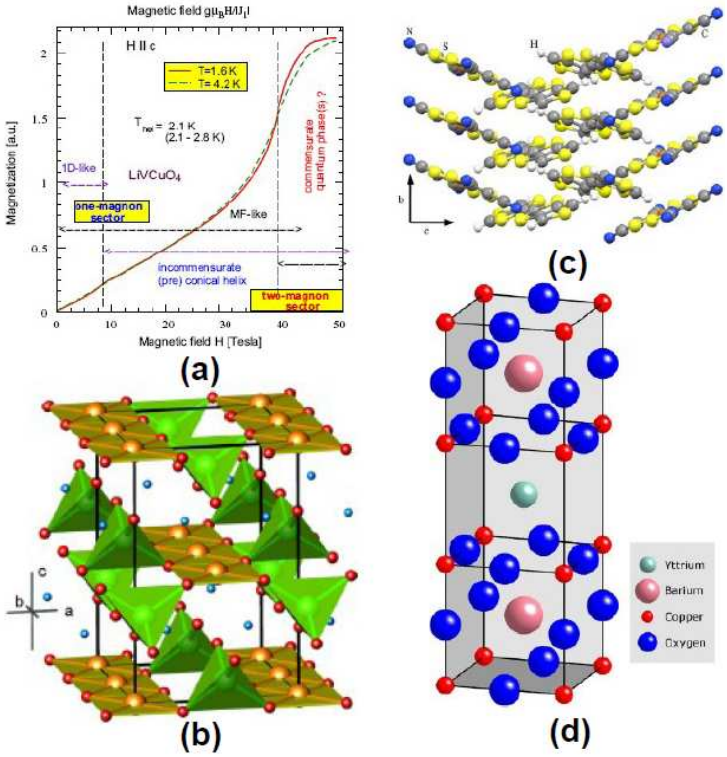

Figure 3.3: (a) Magnetization and (b) structure of $LiCuVO_4$, and structures of (c) $(DTTTF)_2Cu(mnt)_2$, and (d) $YBa_2Cu_3O_7$. [18, 21, 24]

bitals is large. The first three electrons will go into the bottom three orbitals, one at a time, according to Hund's rule and the Pauli principle. If the excitation energy of the electron is less than Δ_0, the subsequent electrons will pair on the bottom (t_{2g}) before filling the top (e_g) levels, in violation of the Aufbau principle. In a weak field ligand, the Δ_0 splitting of the d-orbitals is small. In this case, the fourth electron will fill the higher orbitals before pairing up in the lower levels. Figure 3.4 shows the occupation schemes in both weak and strong field ligands. [37, 38] This strategy can be understood with crystal field theory.

In contrast to oxides, Table 3.1 shows that several of the copper halide systems can be saturated at fields that are relatively low. Examples include $(5IAP)_2CuBr_4{\cdot}2H_2O$, $(C_5H_9NH_3)_2CuBr_4$, $Cu_2(C_5H_{12}N_2)_2Cl_4$ and NH_4CuCl_3. Combining an organic counterion with a halide-containing chromophore, is thus one example of a successful weak field ligand approach. Figure 3.5 shows two examples of such materials, along with their magnetization data. Here, the use of

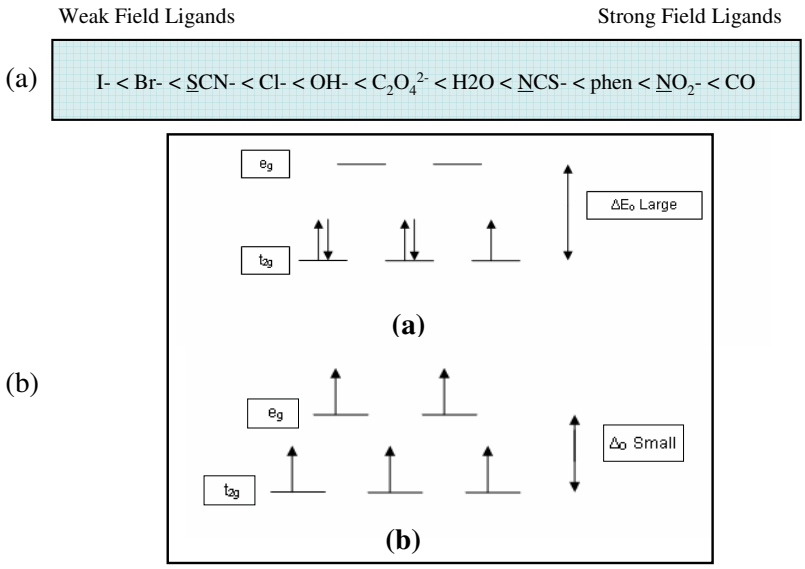

Figure 3.4: A select portion of the spectrochemical series,(a) showing the weak and strong field ligands, [37] coupled with crystal field splitting diagrams, (b) with a strong-field ligand with high energy octahedral splitting of the d-orbitals (a), and a weak-field ligand with low energy octahedral splitting of the d-orbitals (b). [37]

a halide substitute outweighs the use of a dopant, especially since dopants can cause chemical disorder. This is the successful approach we followed in our work.

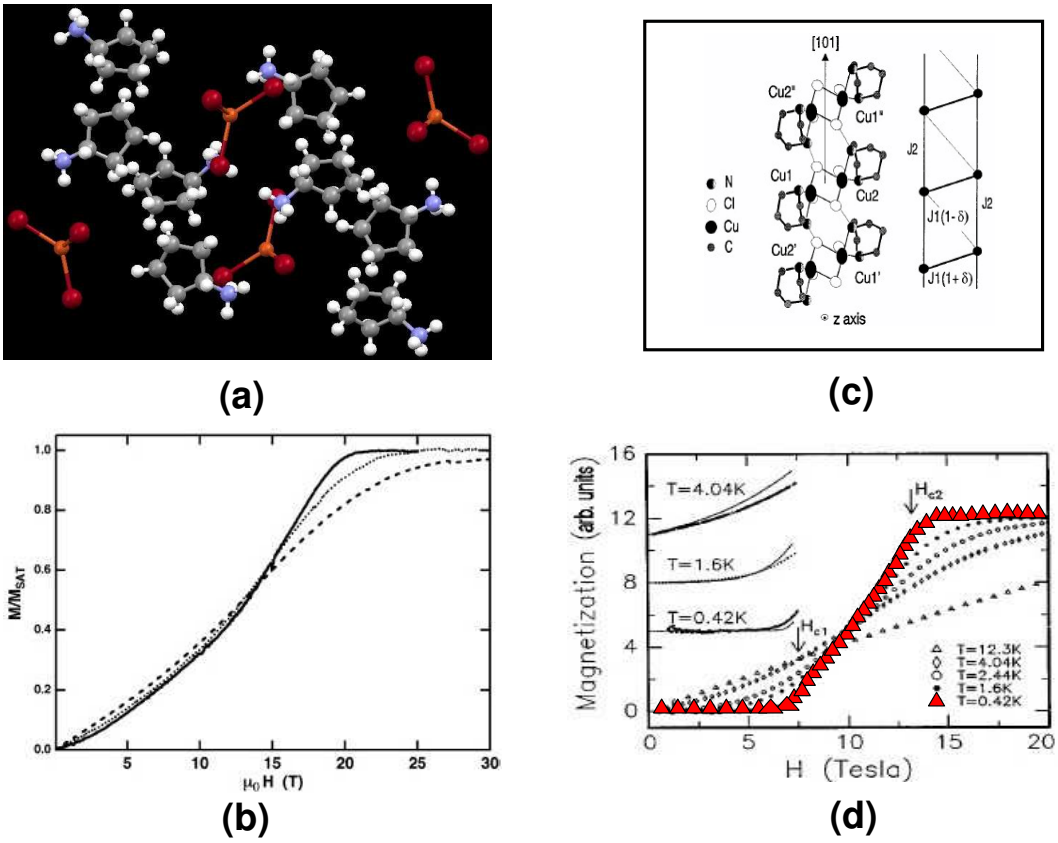

Figure 3.5: Structure (a) and magnetization (b) of $(C_5H_9NH_3)_2CuBr_4$ and structure (c) and magnetization (d) of $Cu_2(C_5H_12N_2)_2Cl_4$. [7, 27–30]

Chapter 4

Understanding the magnetic properties of (2,3-dmpyH)$_2$CuBr$_4$

Theoretical values of H_{c1} and H_{c2} were estimated in advance of the experiments for (2,3-dmpyH)$_2$CuBr$_4$ using several strong rung models [39–42] along with Shapiro's data on exchange interactions and spin gap. [4] Together, these models predict spin gaps (Δ) between 3.56 K and 4.08 K, a lower critical field (H_{c1}) of 2.59 T, and an upper critical field (H_{c2}) between 21.2 T and 36.9 T. Although none of these models are really well-suited for our "strong-rail" system, estimated values are in reasonable agreement with the experimental data, indicating that these models can be extrapolated outside the formal range of their validity.

Greven's model [40] is developed from a Monte Carlo simulation, with the idea of modeling the ideal spin ladder, where $J_\perp/J_\parallel$=1. Using

$$\Delta = 0.41 \mid 2J_\perp \mid, \tag{4.1}$$

we extract a Δ of 3.56 K with minimal parameters. [40] Another model from Batchelor [39] allows us to calculate Δ differently with very limited information. The equation

$$\Delta = J_{\perp} - J_{\parallel} \tag{4.2}$$

gives a value for the spin gap of 4.08. Both estimates are in good agreement with Shapiro's extrapolated value of 3.69 K, obtained from fits to the susceptibility. [4] Using Shapiro's value for Δ and g = 2.12, we can estimate H_{c1} as

$$\Delta = \mu_B g H_{c1}. \tag{4.3}$$

We find $H_{c1} = 2.59$ T. Using this value of H_{c1} and the experimental Δ, we can back calculate the rescaling constant γ as [39]

$$\Delta = J_{\perp} - 4J_{\parallel}/\gamma. \tag{4.4}$$

We find $\gamma = 4.19$, similar to the value for $(5\text{IAP})_2\text{CuBr}_4{\cdot}2\text{H}_2\text{O}$. [39]

An estimate of H_{c2} can be obtained using

$$H_{c2}/\Delta = (1+2)/[(\gamma J_{\perp}/4J_{\parallel}) - 1], \tag{4.5}$$

finding that $H_{c2} = 24.1$ T. Hayward's model provides an independent way of estimating H_{c2} based on the spin gap and $J_{\perp}/J_{\parallel}$. By extrapolating the diagram toward $J_{\perp}/J_{\parallel} = 0.5$, we find

$$H_{c2}/\Delta \approx 10. \tag{4.6}$$

This yields $H_{c2} = 36.9$ T. [41] Finally, the molecular field approximation for the saturation field of an antiferromagnetic compound, H_{c2} can also be estimated as [42]

$$H_{c2} = J_{\perp} + 2J_{\parallel} \tag{4.7}$$

Table 4.1: Theoretical Magnetic Models

Model	Equation	Theoretical Estimates
Eqn. 4.1, Greven [40]	Δ= 0.41 $\|2J_{\perp}\|$	Δ = 3.56 K
Eqn. 4.2, Batchelor [39]	$\Delta = J_{\perp}$ - $J_{\parallel}$	Δ = 4.08 K
Eqn. 4.3, Batchelor [39]	$\Delta = \mu_B g H_{c1}$	H_{c1} = 2.59 T
Eqn. 4.4, Batchelor [39]	$\Delta = J_{\perp}$ - $4J_{\parallel}/\gamma$	γ = 4.19
Eqn. 4.5, Batchelor [39]	$H_{c2}/\Delta = (1+2)/[(\gamma J_{\perp}/4J_{\parallel})-1]$	H_{c2} = 24.1 T
Eqn. 4.6, Hayward [41]	$H_{c2}/\Delta \approx 10$	H_{c2} = 36.9
Eqn. 4.7, deJongh [42]	$H_{c2} = J_{\perp} + 2J_{\parallel}$	H_{c2} = 21.2 T

giving H_{c2}=21.2 T. [42] All of the predictions for these theoretical models are shown in Table 4.1.

In order to test predictions of the models and to evaluate the critical fields, we measured the magnetization of (2,3-dmpyH)$_2$CuBr$_4$ (Figure 4.1). Application of an external magnetic field will close the singlet-triplet gap and induce a moment in the ladder when the Zeeman energy exceeds the gap energy. [28] Because the spin gap is small, low temperatures were needed to fully elucidate its behavior. At the same time, the low values of exchange interactions and spin gap allow the magnetization to be saturated in an experimentally realizable field.

This data demonstrates that the system can indeed be saturated. The elbow at 2.8 T represents H_{c1}, the field necessary to close the spin gap. The magnetic moment on the copper atom saturates, and thus the spins begin to cant. The knee at 29 T correlates with H_{c2}, the field needed to saturate the system. From these experimental values, we were able to extract the average spin gap, Δ = 3.99 K, in good agreement with that in previous literature. [4] Using Eqn. 4.4, we extract a γ value of 4.04, again, a value in good agreement with our theoretical model of 4.19. The lack of other significant features in the experimental magnetization also shows that there no significant magnetic exchange within the molecules,

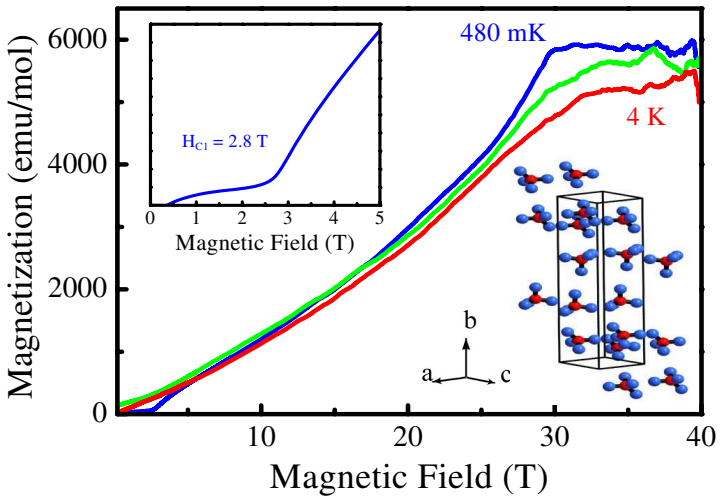

Figure 4.1: Magnetization $\| \ b$ of (2,3-dmpyH)$_2$CuBr$_4$ at 4.2 K, 1.6 K, and 480 mK. The 480 mK data shows H_{c1} and H_{c2} most clearly. Upper inset: close-up view of H_{c1}. Lower inset: 300 K structure of (2,3-dmpyH)$_2$CuBr$_4$. [4] The organic counterions are omitted for clarity.

apart from those interactions that form the spin ladder. [4]

The magnetization of (2,3-dmpyH)$_2$CuBr$_4$ compares well with other copper halide systems. The saturation at 5700 emu/mol is the expected value for a S = $\frac{1}{2}$ system. Table 4.2 shows our system's critical fields compared with several other copper halides. Examining the fields as a group further demonstrates that copper halides, as a group, are ideal for further optical studies, due to their low energy scales.

Table 4.2: Copper Halide Systems and Their Critical Fields

System	Critical Field (H_{c1})	Critical Field (H_{c2})	Reference
$(5IAP)_2CuBr_4\ 2H_2O$	$H_{c1} = 8.3$ T	$H_{c2} = 10.4$ T	[27]
$(C_5H_9NH_3)_2CuBr_4$	$H_{c1} = 2$ T	$H_{c2} = 24$ T	[7, 28]
$(C_5H_{12}N)_2CuBr_4$	$H_{c1} = 6.6$ T	$H_{c2} = 14.6$ T	[26]
$Cu_2(C_5H_{12}N_2)_2Cl_4$	$H_{c1} = 7.5$ T	$H_{c2} = 13.2$ T	[30, 41]
$(2,3\text{-dmpyH})_2CuBr_4$	$\mathbf{H_{c1} = 2.8}$ **T**	$\mathbf{H_{c2} = 29}$ **T**	**This Work**

Chapter 5

Optical and Magneto-Optical Studies of 2,3-$(dmpyH)_2CuBr_4$

5.0.4 Excitation Assignments of the $CuBr_4^{2-}$ Chromophore

Figure 5.1 displays the optical properties of $(2,3\text{-dmpyH})_2CuBr_4$. This graph shows our most interesting data points, the triplet between 1.9 eV $\rightarrow$ to 2.4 eV and the shoulder centered at 3.5 eV. Electronic structure calculations were done on the $CuBr_4^{2-}$ chromophore for studies of a similar material, $(C_5H_9NH_3)_2CuBr_4$. [7] Figure 5.1 shows the electronic structure calculations. The calculations show us that there are five sets of excitations, all relatively independent of polarization. By comparing these calculations with our experimental data, we see that the excitations are a result of the d to d on-site transitions of the $CuBr_4^{2-}$ chromophore. [7] The weak low-energy peaks at $\sim$ 0.58 and 1.04 eV are assigned to the $4B_2 \rightarrow 6A_1$ and $5A_1 \rightarrow 6A_1$ excitations and c and a crystallographic directions, respectively. The triplet at $\sim$ 2.04, 2.21, and 2.35 eV is assigned to the $3B_1$, $3B_2$, $4A_1 \rightarrow 6A_1$, $2B_1$, $2B_2$, $3A_1 \rightarrow 6A_1$, and $1B_1$, $1B_2$, $2A_1 \rightarrow 6A_1$, respectively. The shoulder centered at $\sim$ 3.19 eV is assigned to the $1A_1 \rightarrow 6A_1$ excitation.

The peak centered at 4.59 eV is related to the excitations from filled s orbitals to the

(a)

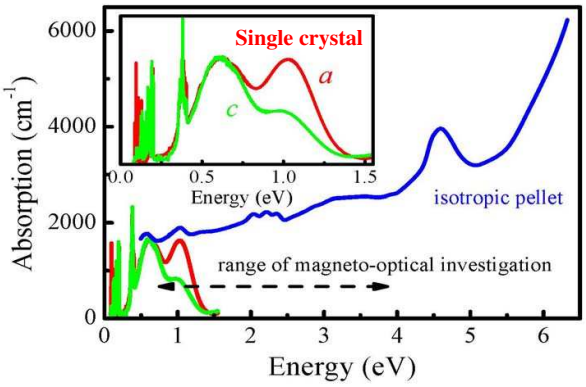

(b)

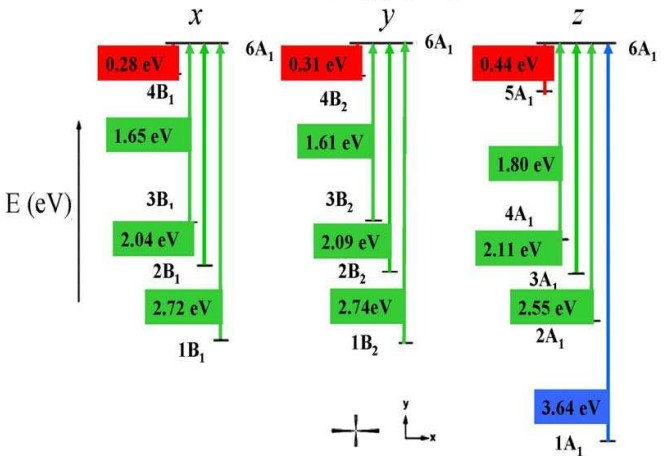

(c)

Experimental Peaks and Theoretical Assignments of 2,3-(dmpyH)$_2$CuBr$_4$

Peak Position (eV)	Spectral Range	Excitation Assignments
0.58 eV	Near Infra-Red	$4B_1 \rightarrow 6A_1$, $4B_2 \rightarrow 6A_1$, $5A_1 \rightarrow 6A_1$
1.04 eV	Near Infra-Red	$4B_1 \rightarrow 6A_1$, $4B_2 \rightarrow 6A_1$, $5A_1 \rightarrow 6A_1$
2.04 eV	Visible	$3B_1 \rightarrow 6A_1$, $2B_1 \rightarrow 6A_1$, $1B_1 \rightarrow 6A_1$
2.21 eV	Visible	$3B_2 \rightarrow 6A_1$, $2B_2 \rightarrow 6A_1$, $1B_2 \rightarrow 6A_1$
2.35 eV	Visible	$4A_1 \rightarrow 6A_1$, $3A_1 \rightarrow 6A_1$, $2A_1 \rightarrow 6A_1$
3.19 eV	Visible	$1A_1 \rightarrow 6A_1$
4.59 eV	Ultraviolet	Organic Counter-ion

Figure 5.1: Optical images, including (a) 4 K absorption of (2,3-dmpyH)$_2$CuBr$_4^{2-}$ in single crystal and isotropic pellet form, (b) electronic structure calculations [7] and (c) tabulated excitations of the CuBr$_4^{2-}$ chromophore.

highest occupied molecular orbital and/or charge transfer between the organic cation and the $CuBr_4{}^{2-}$ anion. [7] These higher energy transitions were not considered in the model calculations. Figure 5.1 shows our assignments based on our experimental peaks. Despite containing the same chromophore, the different organic counterions cause different orbital overlaps. These differences are exhibited in the different values for $J_\perp$, $J_\parallel$, and the spin gap (Δ). [28]

5.0.5 Temperature Dependence in 2,3-$(dmpyH)_2CuBr_4$

Temperature is one way to modify a tunable system. Many systems experience a "hardening" of features as temperature decreases, and a "softening" of features as the temperature increases. In 2,3-$(dmpyH)_2CuBr_4$, several modes "hardened" at low temperature. The most extreme change occurred between 2-2.5 eV, as the triplet feature that appears so clear at low temperature becomes nothing more at a shoulder between 150-200 K (Figure 5.2). Apart from a distinct change in shape, this "hardening" at low temperature and subsequent "softening" at a warmer temperature shows a shift in the peak centers. These changing modes are a result of a weak local distortion of the $CuBr_4{}^{2-}$ chromophore. Table 5.2 shows the positions of the three peaks. Figure 5.2 shows peak position as a function of temperature, and is shaded in the "transition" area.

5.0.6 Field Dependence in 2,3$(dmpyH)_2CuBr_4$

Field-Driven Color Changes

Figure 5.3 displays a close-up view of the magneto-optical absorption of (2,3-dmpyH)$_2$ $CuBr_4$. This pulsed-field data showed a field dependence in the visible range causing a color change in the material at the $^3B_1$, $^2B_1$, $^1B_1 \rightarrow {}^6A_1$, $^3B_2$, $^2B_2$, $^1B_2 \rightarrow {}^6A_1$, $^4A_1$, $^3A_1$, $^2A_1 \rightarrow {}^6A_1$, and $^1A_1 \rightarrow {}^6A_1$ transitions. A field-induced color change, or magnetochromism, has previously

(a)

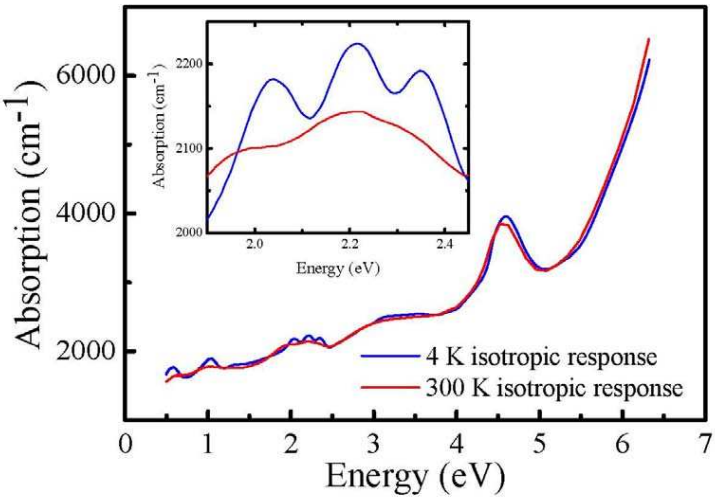

(b)

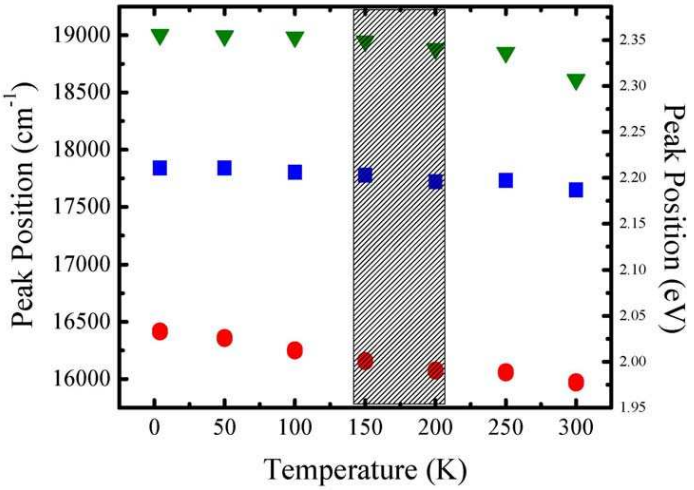

Temperature-Dependent Peak Positions of $CuBr_4^{2-}$

(c)

Temperature (K)	$^3B_1$ $^3B_2 \rightarrow {}^6A_1$ (eV) $^4A_1$	$^2B_1$ $^2B_2 \rightarrow {}^6A_1$ (eV) $^3A_1$	$^1B_1$ $^1B_2 \rightarrow {}^6A_1$ (eV) $^2A_1$
4.2	2.0342	2.2113	2.3561
50	2.0271	2.2112	2.3548
100	2.0136	2.2067	2.3535
150	2.0020	2.2035	2.3490
200	1.9917	2.1964	2.3407
250	1.9898	1.9774	2.3367
300	1.9789	2.1875	2.3072

Figure 5.2: Graphical representations of (a) variable temperature data at 4 and 300 K, showing structural change, (b) and center peak positions for the triplet at varying temperatures. (c) Tabulated peak positions at various temperatures, coupled with their $CuBr_4^{2-}$ chromophore excitations.

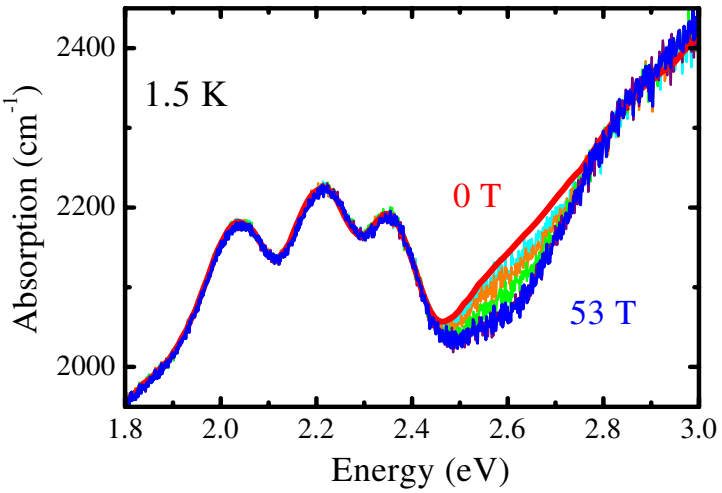

Figure 5.3: Low temperature magneto-optical response of (2,3-dmpyH)$_2$ $CuBr_4$ at 0, 20, 23, 27, 35, and 53 T.

been seen in other systems. These systems include $Cu(HF_2)(pyz)_2BF_4$, $(C_5H_9NH_3)_2CuBr_4$, $Li_{0.9}Mo_6O_{17}$, $(La_{0.4}Pr_{0.6})_{1.2}Sr_{1.8}Mn_2O_7$, $K_2V_3O_8$, and even some superconducting cuprates. [7,8,10,11,44–46] We interpret the color change in our system as an effect of magnetoelastic coupling, which causes a distortion of the $CuBr_4{}^{2-}$ ladder. The spectral shift in our system is quite large, too large to be an effect of Zeeman splitting or simple g factor effects. [47] Zeeman splitting would give splitting of 1.06 x 10^{-21} J, and g factor effects give a result of approximately 2.

Magneto-Optics + Magnetism

To further analyze the magneto-optical effect, we integrated absolute value of the absorption difference, and plotted the area as a function of field. Figure 5.4 shows that the magneto-optics tracks the magnetization. In comparison with the magnetization saturation field, we see that there is a small lag.

This lag is due to a slow lattice response. Looking at Figure 5.4, we see that the optical contrast changes slope around $\sim$ 18 T, as magnetic moment on the copper center saturates, and thus canting begins. The absorption contrast changes slope again around $\sim$ 35 T, when

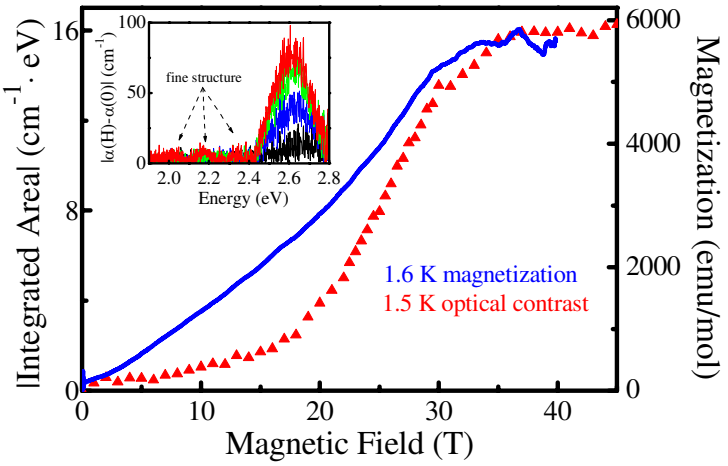

Figure 5.4: Low temperature magneto-optical contrast compared with magnetization data. Inset: close-up view of the absorption difference spectra at $H = 15$, 25, 30, and 52 T.

the system saturates. The lag seen here with the absorption contrast saturation is similar to direct magnetoelastic measurements on another Cu^{2+} centered system, $[Cu(HF_2)(pyz)_2]BF_4$. [8]

The magnetic field causes intramolecular changes to the chromophore, modifying the molecular orbital overlap. This overlap, in turn, causes distortion to the ladder structure, adjusting the $J_\perp$ and $J_\parallel$ values. Since our ladder is constructed from our magnetic component, the Cu^{2+} center of the chromophore, the $J_\perp$ and $J_\parallel$ values changing due to the magnetic field directly affects the ladder, coupling the optical changes to our magnetization data. These changes are interpreted as a result of magnetoelastic coupling in the system.

Chapter 6

Conclusion

In this thesis, I present magnetization, optical, and magneto-optical spectroscopic studies of the S=$\frac{1}{2}$ Heisenberg antiferromagnetic spin ladder, (2,3-dmpyH)$_2$CuBr$_4$. My analysis focuses on using temperature and magnetic field to tune the properties of this system, and interpreting the data in terms of inter/intramolecular effects and magnetoelastic coupling.

Magnetization experiments were performed and scaled to give a saturation magnetization around approximately 5700 emu/mol, the estimated value for an S = $\frac{1}{2}$ system. Critical fields appeared at 2.8 T (H_{c1}) and 29 T (H_{c2}). These experimental results correlated well with the range of theoretical estimates calculated prior to the experiment, from extrapolated models designed for "strong rung" spin ladder systems. The agreement with the theoretical values shows that these "strong rung" models are useful outside of their original range of validity. Using these theoretical models with our experimental values, we extracted values of $\Delta = 3.99$ K and $\gamma = 4.04$. The variable temperature data showed "hardening" of modes with low temperature, and a shift in peak positions. Electronic structure calculations were done on the $CuBr_4{}^{2-}$ chromophore, and assigned to our experimental data. The field-driven magnetic ordering transition yielded a color change, associated primarily with the $1A_1 \rightarrow 6A_1$ transition, but also caused by shifting in the triplet structure centered at ~ 2.25 eV. The shift

associated with the color change is quite large, too large to be an effect of Zeeman splitting or caused by g factor effects. [47] Plotting the optical contrast against the magnetization, we see that the color change (optical contrast) tracks the magnetization. We interpret this result in terms of magnetoelastic effects. The optics, thus, are sensitive to the transition to the ferromagnetic state.

We conclude that (2,3-dmpyH)$_2$CuBr$_4$, a "strong rail" copper halide spin ladder has modest magnetic exchanges and can be saturated with conventional magnets. Complimentary magneto-optics show that the field causes a spectral shift, likely with a magnetoelastic mechanism. After calculating the absorption contrast and plotting it with the magnetization, we see that the optics track the magnetization. These properties demonstrate that (2,3-dmpyH)$_2$CuBr$_4$ is a good model for copper oxide systems, and that the interplay between charge, spin, and magnetism is alive and well in other functional materials.

Bibliography

Bibliography

[1] D. W. Murphy, S. Sunshine, R. B. van Dover, R. J. Cava, B. Batlogg, S. M. Zahurak, and L. F. Schneemeyer, Phys. Rev. Lett. **58** 1888 (1987).

[2] E. Dagotto and T. M. Rice, Science **271**, 618 (1996)

[3] J. G. Bednorz and K. A. Mueller, Z. Phys. B **64**, 189 (1986).

[4] A. Shapiro, C. P. Landee, M. M. Turnbull, J. Jornet, M. Deumal, J. J. Novoa, M. A. Robb, and W. Lewis, J. Am. Chem. Soc. **129**, 952 (2007).

[5] T. Hong, M. Kenzelmann, M. M. Turnbull, C. P. Landee, K. P. Schmidt, G. S. Uhrig, Y. Qiu, C. Broholm, and D. Reich, Phys. Rev. B **74**, 094434 (2006).

[6] C. Broholm, T. Hong, Unpublished Results.

[7] J. D. Woodward, J. Choi, and J. L. Musfeldt, J. T. Haraldsen, X. Wei, H.-J. Koo, D. Dai, M.-H. Whangbo, C. P. Landee, and M. M. Turnbull, Phys. Rev. B **71**, 174416 (2005).

[8] J. L. Musfeldt, L. I. Vergara, T. V. Brinzari, L. C. Tung, Y. J. Wang, J. A. Schlueter, J. L. Manson, C. Lee, and M.-H. Whangbo, Phys. Rev. Lett. (submitted).

[9] F. M. Woodward, A. S. Albrecht, C. M. Wynn, C. P. Landee, and M. M. Turnbull, Phys. Rev. B **65**, 144412-1 (2002).

[10] M. V. Klein and G. Blumberg, Science **283**, 42 (1999).

[11] J.E. Hirsch, Physica C **201**, 347 (1992).

[12] F. Wooten, *Optical Properties of Solids* (Academic Press, New York, 1972).

[13] H. K. Ng, Y. J. Wang, *In Physics Phenomena at High Magnetic Field-II*;Z. Fisk, L. Gor'kov, D. Meltzer, R. Schrieffer, Eds.; World Scientific: Singapore, 1995.

[14] G.-F. Li, *FTIR Spectroscopic Studies of Spin-Peierles Materials*, Master's Thesis, State University of New York at Binghamton, 1997.

[15] Z.-T. Zhu, *Spectroscopic Studies of Charge Density Wave Bronzes and Fullerene Polymers*, Ph. D Dissertation, State University of New York at Binghamton, 2001.

[16] F. W. Billmeyer and M. Saltzman, *Principles of Color Technology, 3rd Ed.*, Wiley, New York (2000).

[17] J. L. Musfeldt, D. B. Tanner, and A. J. Paine, J. Opt. Soc. Am. A **10** 2648 (1993).

[18] S.-L. Drechsler, J. Richter, R. Kuzian, J. Malek, N. Tristan, B. Buchner, A. S. Moskvin, A. A. Gippius, A. Vasiliev, O. Volkova, A. Prokofiev, H. Rakoto, J.-M. Broto, W. Schnelle, M. Schmitt, A. Ormeci, C. Loison, and H. Rosner, J. Magn. and Magn. Mater. **316**, 306 (2007).

[19] V. V. Moshchalkov, L. Trappeniers, and J. Vanacken, Europhys. Lett. **46**, 75 (1999).

[20] M. Azuma, Z. Hiroi, M. Takano, Phys. Rev. Lett. **73**, 3463 (1994).

[21] T. Sekitani, N. Miura, S. Ikeda, Y. H. Matsuda, and Y. Shiohara, Physica B **346-347**, 319 (2004).

[22] H. P. Roeser, F. Hetfleisch, F. M. Huber, M. F. von Schoernermark, M. Stepper, A. Moritz, and A. S. Nikoghosyan, Acta Astronautica **62**, 733 (2008)

[23] H. Nojiri, Y. Shimamoto, N. Miura. M. Hase, K. Uchinokura, H. Kojima, I. Tanaka, and Y. Shibuya, Phys. Rev. B **52**, 749 (1995).

[24] J. L. Musfeldt, S. Brown, S. Mazumdar, R. T. Clay, M. Mas-Torrent, C. Rovira, J. C. Dias, R. T. Henriques, and M. Almeida, Solid State Sci. **10**, 1740 (2008).

[25] X. Ribas, M, Mas-Torrent, A. Perez-Benitez, J. C. Dias, H. Alves, E. B. Lopes, R. T. Henriques, E. Molins, I. C. Santos, K. Wurst, P. Foury-Leylekian, M. Almeida, J. Veciana, and C. Rovira, Adv. Funct. Mater. **15**, 1023 (2005)

[26] B. C. Watson, V. N. Kotov, and M. W. Meisel, Phys. Rev. Lett., **86**, 5168 (2001).

[27] C. P. Landee, M. M. Turnbull, C. Galeriu, J. Giantsidis, and F. M. Woodward, Phys. Rev. B **63**, 100402 (2001).

[28] R. D. Willett, C. Galeriu, C. P. Landee, M. M. Turnbull, and B. Twamley, Inorg. Chem. **43**, 3804 (2004).

[29] C. A. Hayward, D. Poilblanc, and L. P. Levy, Phys. Rev. B **64**, R12649 (1996)

[30] G. Chaboussant, P. A. Crowell, L. P. Levy, O. Piovesana, A. Madouri, and D. Mailly, Phys. Rev. B **55**, 3046 (1997).

[31] E. Bordas, C. de Graaf, and R. Caballol, Phys. Rev. B **71**, 045108 (2005).

[32] H. Tanaka, W. Shiramura, T. Takatsu, B. Kurniawan, M. Takahashi, K. Kamishima, K. Takizawa, H. Mitamura, and T. Goto, Physica B **246-247**, 230 (1998).

[33] W. Shiramura, K. Takatsu, H. Tanaka, K. Kamishima, M. Takahashi, H. Mitamura, and T. Goto, J. Phys. Soc. Jpn. **66**, 1900 (1997).

[34] I. Bose, arXiv: cond-mat/0107399v1 19 Jul 2001

[35] T. Barnes, E. Dagotto, J. Riera, and E. S. Swanson, Phys. Rev. B **47**, 3146 (1993).

[36] T. Hikihara, and A. Furusaki, Phys. Rev. B **63**, 134438-1 (2001)

[37] F. A. Cotton, Chemical Applications of Group Theory, New York, (1963).

[38] G. L. Miessler, and D. A. Tarr, Inorganic Chemistry, Upper Saddle River, (1999)

[39] M. T. Batchelor, X.-W. Guan, A. Foerster, and H.-Q. Zhou, New J. Phys. **5**, 107 (2003).

[40] M. Greven, R. J. Birgeneau, and U.-J. Wiese, Phys. Rev. Lett. **77**, 1865 (1996).

[41] C. A. Hayward, D. Poilblanc, and L. P. Levy, Phys. Rev. B **54**, 649 (1996).

[42] L. J. de Jongh, A. R. Miedema, Advances in Physics **23**, 1 (1974).

[43] P. A. Goddard, J. Singleton, R. D. McDonald, T. Lancaster, S. J. Blundell, F. L. Pratt, S. Cox, J. L. Manson, H. I. Southerland, and J. A. Schlueter, arXiv:0803.4169v1 [cond-mat.str-el] 28 Mar 2008

[44] R. C. Rai, J. Cao, J. L. Musfeldt, D. J. Singh, X. Wei, R. Jin, Z. X. Zhou, B. C. Sales, and D. Mandrus, Phys. Rev. B **73**. 075112 (2006).

[45] J. Choi, J. D. Woodward, J. L. Musfeldt, J. T. Haraldsen, X. Wei, M. Apostu, R. Suryanarayanan, and A. Revcolevschi, Phys. Rev. B **70**, 064425 (2004).

[46] J. Choi, J. D. Woodward, J. L. Musfeldt, X. Wei, M.-H. Whangbo, J. He, R. Jin, and D. Mandrus, Phys. Rev. B **70**, 085107 (2004).

[47] R. D. MacDonald, Unpublished Results.

Vita

Jessica White was born in Reading, Pennsylvania. She attended McGill University in Montreal, Quebec, Canada between 1999 and 2003, where she received a B. A. degree, majoring in Foreign Language and Chemistry. In August 2006, she enrolled as a graduate student in the Physics Department at the University of Tennessee, Knoxville. She joined Dr. Janice Musfeldt's group to begin research in the field of spectroscopic investigations of a quantum spin ladder. Jessica White received a Master's Degree in Physics from the University of Tennessee in May 2009.